

Seismicity and Active Faulting around the Metropolitan Area of Athens, Greece

Kostas I. Konstantinou^{*1}, Vasiliki Mouslopoulou², and Vasso Saltogianni³

ABSTRACT

The existence of active faults near large cities poses significant risk to the life and property of its inhabitants as well as to its public infrastructure. Here, we investigate the interplay between seismicity, active faulting, and interseismic strain accumulation within a radius of ~ 50 km from the metropolitan area of Athens, the capital of Greece. We find that during the period 2011–2018, a total of 4722 earthquakes were recorded, the majority of which had local magnitudes < 3.0 with only four events being of moderate magnitude (M_L 4.1–4.3). Precise relative locations with horizontal and vertical errors of ≤ 1 and 2 km, respectively, were obtained for 2666 of these events using the double-difference algorithm. Earthquake relocation was compared to the surface traces of 31 active and 49 “less-active” normal faults drawn from high-resolution (~ 5 m pixel size) digital elevation models and complemented by analysis of geodetic data from 30 permanent Global Positioning System (GPS) stations. Joint analysis of these datasets suggests that microseismicity mostly clusters along the “less-active” faults, whereas the faults associated with impressive postglacial scarps (indicating recent activity) and historic seismicity are mostly quiet. Interestingly, GPS data indicate that both fault types currently accumulate elastic strain that ranges from 0.5 to 2.3 mm/yr. Based on their estimated rupture area, more than half of the recorded faults ($N = 54$) are capable of generating earthquakes with moment magnitudes between 6.0 and 6.6. Although some of these sources are characterized by impressive postglacial scarps, many others have long earthquake recurrence intervals (i.e., have not ruptured during the past ~ 16 ka) and are associated with intense microseismicity and elastic strain accumulation, calling for future investigations on their seismogenic potential.

KEY POINTS

- We compare patterns of seismicity, active faulting, and strain accumulation in the Athens metropolitan area.
- We find more seismic sources capable of producing earthquakes with M_w 6.0–6.6 than previously thought.
- Faults with long recurrence intervals that have not ruptured for millennia currently accumulate strain and experience intense microseismicity.

[Supplemental Material](#)

INTRODUCTION

Throughout its long history, Greece has been subjected to high levels of seismicity, occasionally climaxing in large earthquakes that result in damages and loss of life (Papazachos and Papazachou, 2003). The main geodynamic process that drives this seismic activity is the subduction of the African lithosphere beneath Eurasia along the Hellenic subduction zone (Fig. 1a). Slab rollback, which has been ongoing since the Oligocene, promotes the gravitational spreading of the upper plate, resulting in widespread extension that is expressed as normal

faulting (Hatzfeld *et al.*, 1997; Meijer and Wortel, 1997; Martinod *et al.*, 2000; Goldsworthy *et al.*, 2002; Konstantinou *et al.*, 2016; Veliz *et al.*, 2018). The subduction also results in the generation of intermediate-depth earthquakes whose hypocenters form a Wadati–Benioff zone along the southern Aegean (Fig. 1a). Although, from time to time, there are intermediate-depth events large enough to cause damage (see, e.g., Konstantinou *et al.*, 2006), the main source of seismic hazard comes from large shallow (<15 km) earthquakes that occur more frequently. Large cities are vulnerable to such earthquakes that nucleate at nearby faults (Talebian *et al.*, 2016), and this is particularly true for a metropolitan city like Athens, the capital of Greece.

The city of Athens has experienced several large earthquakes during the past 2300 yr; however, none of them was

1. Department of Earth Sciences, National Central University, Jhongli, Taiwan;
2. Institute of Geodynamics, National Observatory of Athens, Athens, Greece;
3. GeoForschungsZentrums (GFZ), Potsdam, Germany

*Corresponding author: kkonst@ncu.edu.tw

Cite this article as Konstantinou, K. I., V. Mouslopoulou, and V. Saltogianni (2020). Seismicity and Active Faulting around the Metropolitan Area of Athens, Greece, *Bull. Seismol. Soc. Am.* **XX**, 1–18, doi: [10.1785/0120200039](https://doi.org/10.1785/0120200039)

© Seismological Society of America

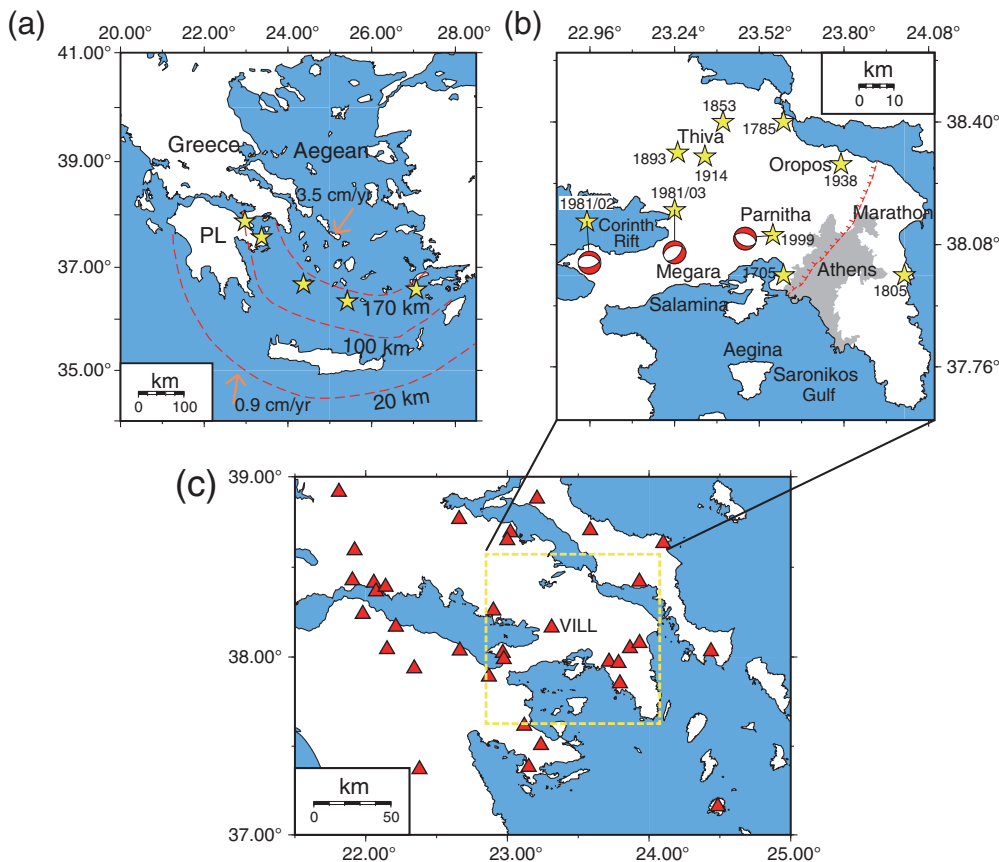


Figure 1. (a) General tectonic setting of the Aegean area. Arrows indicate the motion of tectonic plates and dashed lines represent the isodepth curves of the Wadati–Benioff zone (after Papazachos *et al.*, 2000). Stars give the locations of the main volcano centers. (b) Historical seismicity around the Athens metropolitan area. Stars indicate the epicenters of large (≥ 6.0) earthquakes during the past 300 yr adopted from the catalog of Papazachos and Papazachou (2003). Focal mechanisms of the three most recent events were taken from the Global Centroid Moment Tensor (Global CMT) database. The shaded area gives the extent of the Athens metropolitan area, and the dashed line represents the detachment that separates the sedimentary formations in the west from the metamorphic rocks in the east (after Grützner *et al.*, 2016). (c) Map of the Hellenic Unified Seismic Network (HUSN) seismic stations that were utilized in this study shown as triangles. The dashed square indicates the extent of the study area. PL, Peloponnese. The color version of this figure is available only in the electronic edition.

strong enough so as to destroy its ancient monuments (Ambraseys and Psycharis, 2012). A look into the historic seismicity around Athens shows that several moderate-to-large events have occurred in the past 300 yr at epicentral distances of up to tens of kilometers from the city center (Fig. 1b). Earthquakes that occurred during the preinstrumental period are characterized by highly uncertain epicentral locations and magnitudes that have been estimated based on the available macroseismic information. In this sense, historic accounts confirm that the events in 1705 and 1805 probably exhibited magnitudes around 6.0 and caused some damage to buildings (Papazachos and Papazachou, 2003), even though their uncertain locations do not allow correlation with any known active fault. The instrumental period started in Greece in 1911 with the installation of the first seismometer with two horizontal components (Papazachos and Papazachou, 2003) and even

though earthquake locations still had large uncertainties, magnitudes could be estimated more accurately. During this period, two $\sim M_w 6$ events occurred: the 1914 Thiva and the 1938 Oropos earthquakes (Fig. 1b). Although these events caused heavy damage locally (maximum intensity VIII+ in Thiva and VIII in Oropos according to Papazachos and Papazachou, 2003), they affected little the city of Athens. Similarly, the earthquakes in February and March 1981 ruptured synthetic and antithetic normal faults at the eastern end of the Corinth rift, and despite their large moment magnitudes (6.6 and 6.2, respectively), they caused little damage to Athens as well (maximum intensity IX+ about 45 km away from Athens according to Papazachos and Papazachou, 2003). Thus, the historic seismicity had hitherto suggested that Athens had not suffered significant damage and/or casualties from nearby earthquakes.

On 7 September 1999, this false impression of “seismic safety” came to an abrupt end when an earthquake with moment magnitude 6.0

occurred only 15 km away from the city center (Fig. 1b). The earthquake ruptured a normal fault along the southern foothills of Mt. Parnitha that was previously thought to be inactive and had no clear surface expression (Pavlidis *et al.*, 2002; Ganas *et al.*, 2004). Subsequent studies revealed a complex coseismic slip distribution of shallow and deeper patches with the rupture propagating toward the city of Athens (Baumont *et al.*, 2002, 2004; Papadimitriou *et al.*, 2002; Roumelioti, Dreger, *et al.*, 2003; Roumelioti, Kiratzi, *et al.*, 2003; Roumelioti *et al.*, 2004). The western part of the city was severely damaged (maximum intensity IX) with many collapsed buildings that caused significant loss of life (143 deaths) as well as destruction of property (100,000 people became homeless; Tselentis and Zahradnik, 2000). The distribution of damage was not only controlled by the rupture directivity and local site effects, but also by an old

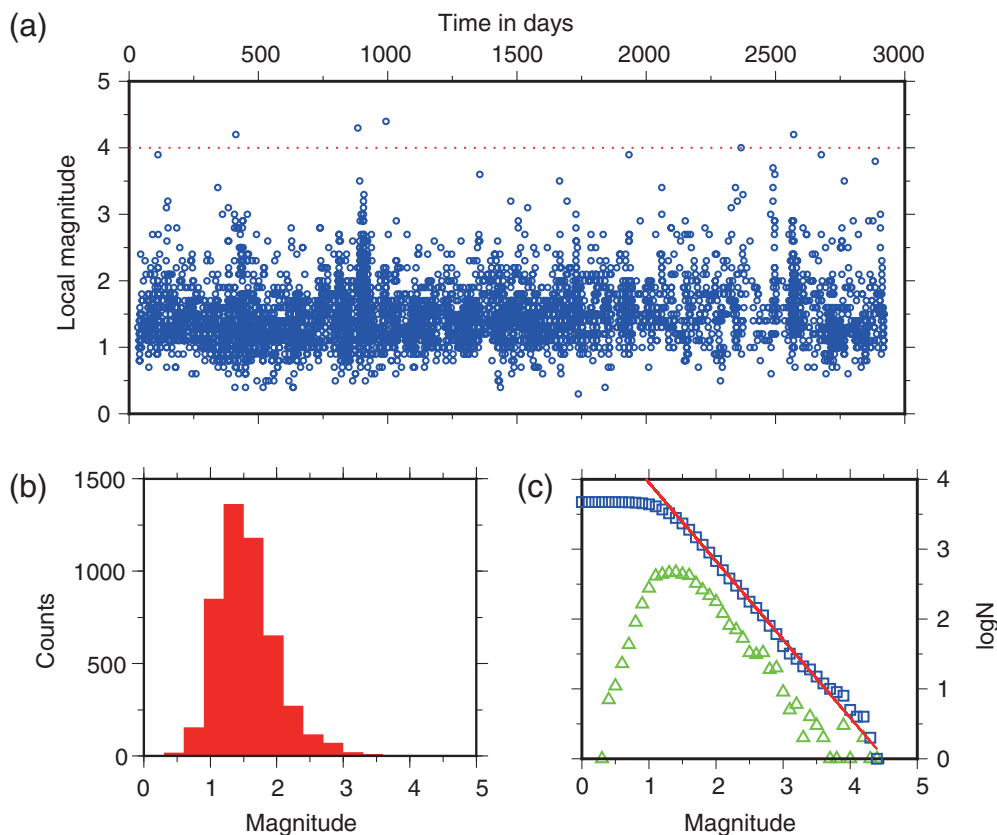


Figure 2. (a) Plot of local magnitude of all events during 2011–2018 as a function of time. The dashed line indicates the threshold of magnitude 4.0, above which only four events have been recorded, (b) histogram of the distribution of local magnitudes for the events included in (a), and (c) calculation of the b -value using a frequency–magnitude plot. Squares indicate the values of cumulative magnitude distribution, whereas triangles represent the noncumulative one. The line has a slope equal to the computed b -value (1.12 ± 0.02). The color version of this figure is available only in the electronic edition.

north-northeast–south-southwest tectonic detachment that dissipated the eastward propagation of seismic energy (Lekkas, 2001). This detachment is a well-known geological feature (Fig. 1b) that separates alpine sedimentary formations in the west from exhumed metamorphic rocks in the east (Papanikolaou and Papanikolaou, 2007; Krohe *et al.*, 2010). The 1999 earthquake showed in a dramatic way that a proper seismic hazard assessment for the city of Athens requires the inclusion of all individual seismogenic sources (i.e., active faults), even those with unclear or subtle surface expression, up to tens of kilometers from the city center.

This work investigates the seismicity within a radius of about 50 km from the city of Athens during the past 8 yr (2011–2018) and its relationship with the distribution of active faulting and interseismic strain accumulation, to obtain a more complete picture of the seismic hazard posed to the capital of Greece. Our analysis starts with the estimation of a minimum 1D velocity model and the calculation of absolute locations for all selected earthquakes. The double-difference algorithm is utilized to enhance the resolution of the absolute locations.

The seismicity distribution is then correlated with fault patterns derived from the analysis of a high-resolution (~ 5 m) digital elevation model (DEM) and strain rates calculated from available geodetic data, highlighting the potential in better characterizing seismic hazard when datasets that span different timescales are combined. Expected moment magnitude for each identified fault is eventually calculated using empirical relationships that take into account the fault length and the seismogenic layer thickness.

EARTHQUAKE DATA AND MAGNITUDE DISTRIBUTION

Seismic activity in the Greek region is monitored by the Hellenic Unified Seismic Network (HUSN), which consists of more than 120 stations equipped with different types of three-component seismometers (Trillium 120P, STS-2, CMG-40T, CMG-3ESP, KS2000, and Le3D-20s). The data recorded by HUSN are

relayed to the Institute of Geodynamics, National Observatory of Athens (NOA), where it is routinely processed. Routine processing of recorded waveforms involves manual picking of arrival times, event location using a simple velocity model of two layers over a half-space, and calculation of local magnitude. For the purpose of this study, we utilized data from 33 HUSN stations (National Observatory of Athens [NOA] Institute of Geodynamics, Athens, 1997) that offer good azimuthal distribution around the broader Athens area (Fig. 1c). We focus on the time period from early 2011 until the end of 2018, period over which the best-quality data may be obtained, yielding a total of 4722 events. The manual picks done by the NOA staff were carefully checked and repicking was performed whenever necessary. A plot of the local magnitude as a function of time reveals that the vast majority of earthquakes has a magnitude below 3.0, essentially representing microseismicity (Fig. 2a,b). We further estimated for our dataset the magnitude of completeness by applying the maximum curvature criterion, as implemented by Woessner and Wiemer (2005) and the b -value using the maximum-likelihood

method (Aki, 1965; Fig. 2c). The magnitude of completeness was found equal to 1.6, which is lower than the average value for HUSN (~ 2.0) reported by D' Alessandro *et al.* (2011). This difference should probably be attributed to the six stations that are located close to Athens (Fig. 1c) and allow the identification and location of earthquakes smaller than magnitude 2.0. The computed b -value is equal to 1.12 (± 0.02), which is consistent with the extensional deformation observed around Athens and also implies relatively low-tectonic stress (Schorlemmer *et al.*, 2005).

METHODOLOGY AND RESULTS

Optimum velocity model and earthquake relocation

Our analysis begins by deriving a minimum 1D velocity model with station delays for our study area using the Velest software package (Kissling *et al.*, 1994). For this purpose, we selected a total of 530 events with 15 or more picked phases, azimuthal gap of 90° or less, and root mean square (rms) residual lower than 0.3 s. Station VILL (see Fig. 1c), which is installed on limestone, was selected as the reference station owing to its location approximately in the center of the network and the large number of phases it recorded. In an effort to probe as much as possible the solution space, we constructed 60 initial P -wave velocity models (Fig. 3a). These models consisted of layers 2 km thick down to a depth of 20 km, and 5 km thick down to 30 km, whereas their velocities were randomly assigned, under the constraint that their values will always increase with depth. Initially, we inverted only the P -phase travel times because they constituted the majority of the measurements and their picking errors are expected to be smaller. From the initial 60 models, seven of them yielded the lowest rms residual of about 0.23 s (Fig. 3a) and exhibited a high degree of similarity in the depth range of 4–20 km. This also indicates that these velocity models are not well constrained outside this depth range, a suggestion that is supported by the distribution of the ray density as a function of depth (Fig. 3b). The average of these seven models was used to produce the final P -wave velocity model that was kept fixed when inverting the S -phase travel times. Figure 3c,d shows the final velocity model along with the depth distribution of the V_P/V_S ratio. There seems to be good correlation between our minimum 1D velocity model and the P -wave model of Drakatos *et al.* (2002) that was derived from the aftershocks of the 1999 Athens earthquake. We further performed a series of robustness tests, as suggested by Kissling (1995). In the first test, we checked the agreement between the station delays and the near-surface geology at the site in which each station is installed. Indeed, we observed that the majority of the delays are either negative or close to zero, which reflects the fact that most stations are installed on hard rocks (mostly limestone). In the second test, we randomly perturbed by ± 7 km the initial hypocentral coordinates of the selected events before inverting again their travel times. The results show that the majority of the events were relocated close to their original locations, and that

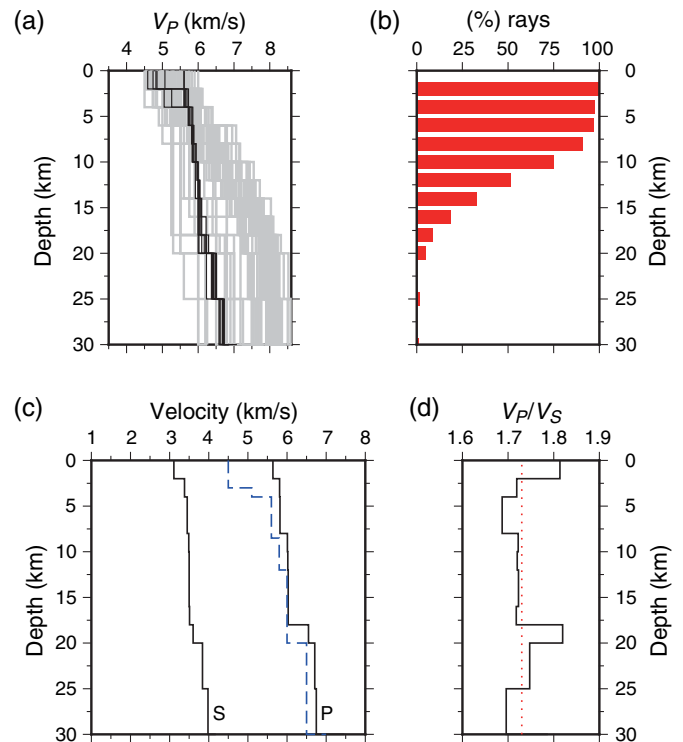


Figure 3. Summary of the results obtained from the inversion of travel times using Velest. (a) Plot of the initial P -wave velocity models shown as gray lines and the final models with the lowest root mean square (rms) residual shown as black lines, (b) frequency distribution of rays (in percentage) as a function of depth, (c) plot as a function of depth of final P - and S -wave velocity models. The dashed line represents the P -wave velocity model of Drakatos *et al.* (2002) that was derived previously for the study area, (d) plot of V_P/V_S ratio as a function of depth derived from the final models. The dotted line indicates the V_P/V_S value that is equal to 1.73. The color version of this figure is available only in the electronic edition.

the velocity model obtained from the perturbed events is very similar to the final velocity model. Figures S1–S3, available in the supplemental material to this article, depict the results of these tests.

The nonlinear probabilistic algorithm NonLinLoc (Lomax *et al.*, 2000, 2009) was employed to calculate absolute earthquake locations using the minimum 1D velocity model and the corresponding station delays. The reconstruction of the posterior probability function for each event was achieved by utilizing the OctTree search algorithm (Lomax and Curtis, 2001) for sampling the solution space. The equal differential time likelihood function (Font *et al.*, 2004), formed from the differences of residuals at station pairs, was also used as it could help to further constrain the locations. Each event that was located in this way had a minimum of eight picked phases of which at least one of them was an S phase. The diagonal elements of the covariance matrix were utilized to calculate uncertainties of the absolute locations as in Maleki *et al.* (2013). In the horizontal direction, the average uncertainty was 2.2 km (± 3.7 km), and in the vertical direction, it was

3.2 km (± 1.8 km). A comparison with routine locations provided by NOA shows a similar depth distribution with a sharp peak at 12 km (Fig. S4). On the other hand, the rms residuals of NonLinLoc locations have an average value of 0.23 s (± 0.12 s), and their distribution is skewed toward smaller values compared to the rms residuals of NOA (Fig. S5). The spatial distribution of the obtained absolute locations can be seen in Figure 4 as a function of hypocentral depth and horizontal as well as vertical uncertainties. Seismicity concentrates along the eastern Corinth rift and the Parnitha region, although there is also significant seismicity in the Saronikos Gulf near the islands of Salamina and Aegina. Fewer earthquakes occur to the north of Athens, such as near the area of the 1938 Oropos earthquake, along the southern Evoikos Gulf and to the east of Athens. We observe that vertical uncertainties become larger than 5 km in areas that are far from seismic stations (e.g., Saronikos Gulf, Fig. 4c). In such cases, the closest station is situated at a distance much larger than the focal depth of these events, not allowing an accurate determination of hypocentral depth (Gomberg *et al.*, 1990).

To improve the spatial resolution of the absolute locations, we also calculated relative locations by applying the double-difference method (Waldhauser and Ellsworth, 2000). We calculated catalog differential travel times by allowing a separation distance of 10 km and also required that each event is connected with 10 of its neighbors. Two events were considered strongly linked when at least eight phase pairs were found, as suggested by Waldhauser (2001). A total of 221,267 *P*-phase and 124,515 *S*-phase pairs were finally built that produced an average of 11 links per event pair, while their average offset was about 3 km. We utilize the newly derived *P*-wave velocity model with a V_p/V_s ratio of 1.73 (Kaviris *et al.*, 2018) for calculating theoretical differential travel times. The inversion problem was solved using the conjugate gradients method (least-squares [LSQR]) with a damping factor of 80 that yielded condition numbers between 40 and 80, and a total of 3026 events were finally relocated. A bootstrap approach was used to assess uncertainties, in which first a random perturbation was drawn from a Gaussian distribution with a standard deviation equal to the median value of the residuals of each event. This was then added to the travel times of each event to replicate the location variability owing to picking errors (see Shearer, 1997). This process was repeated 200 times for the purpose of obtaining perturbed relative locations for each event. The median shift in longitude and latitude and hypocentral depth of all these locations was then considered as an estimate of the relative error. From the 3026 initially relocated events, we selected 2666 events that exhibited horizontal uncertainties of ≤ 1 km and vertical ones of ≤ 2 km. For these events, the average uncertainty in longitude is 0.32 km (± 0.29 km), in latitude is 0.28 km (± 0.32 km), and the average vertical uncertainty is 1.15 km (± 1.97 km). Figure S5 shows histograms of these uncertainties, and Figure S6 shows

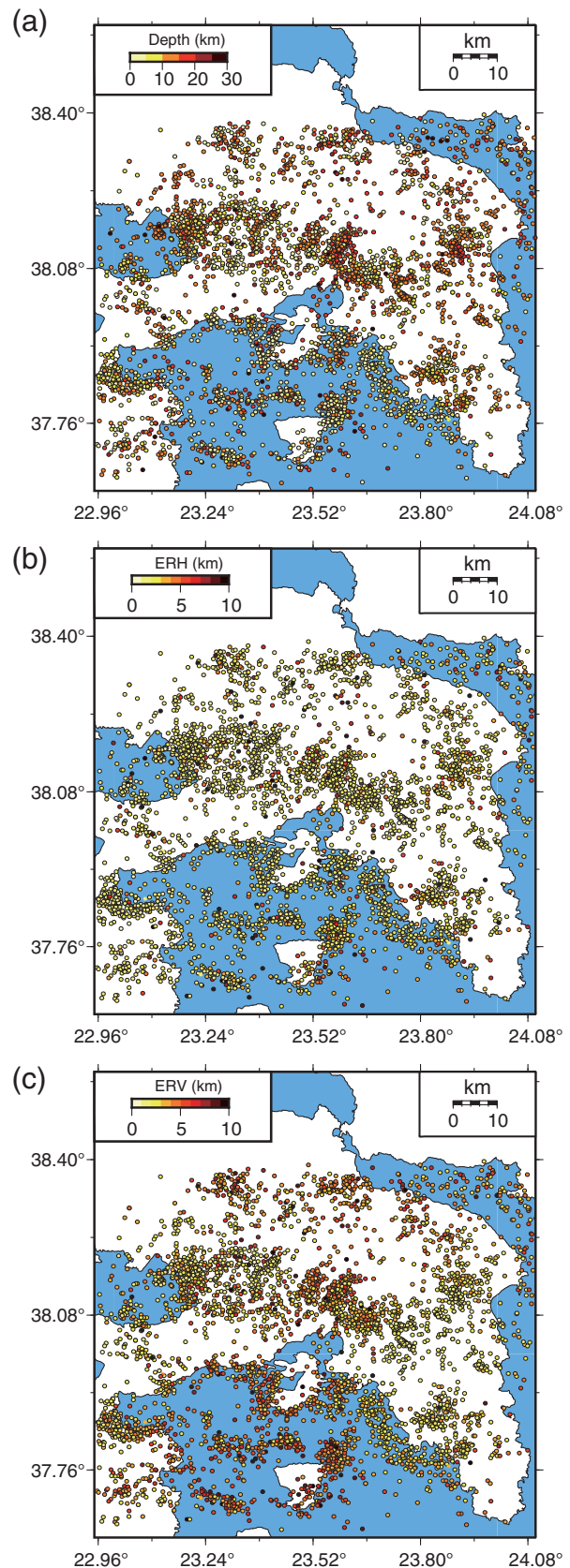
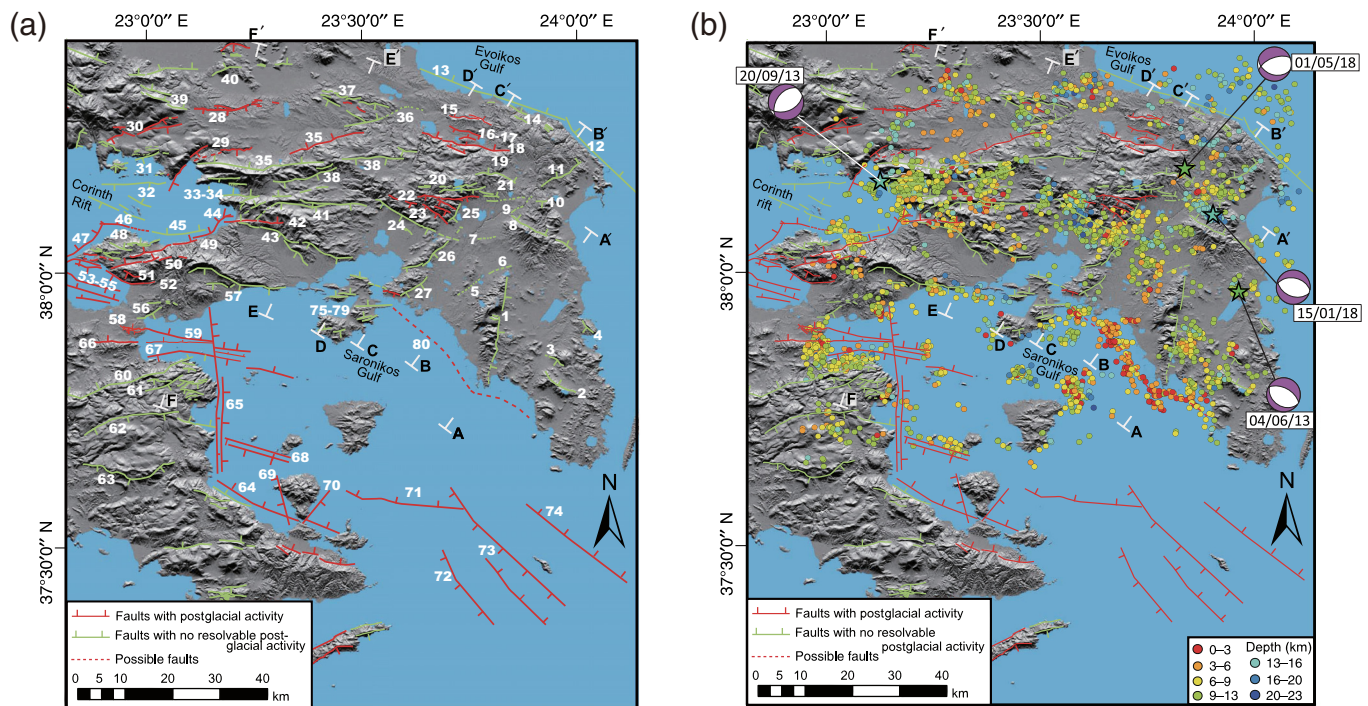


Figure 4. Map of absolute locations obtained from NonLinLoc shown as circles shaded according to (a) hypocentral depth, (b) horizontal error (ERH), and (c) vertical error (ERV). The color version of this figure is available only in the electronic edition.



the uncertainties in map view. Overall, the relocated earthquakes have local magnitudes of 3.0 or less; however, there are four events with local magnitudes between 4.1 and 4.3 that were felt in Athens and the surrounding areas. Three of them are located to the east of Athens and one originated in the eastern Corinth rift, very close to the coast (for locations, see stars in Fig. 5b).

Identification and classification of faults

An increasing body of evidence suggests that fault lengths are often underestimated, in some cases by more than 50% (Wesnousky, 2008; Mouslopoulou *et al.*, 2012; Nicol *et al.*, 2016; Biasi and Wesnousky, 2017). Improved estimates of fault lengths may be particularly important, because this is a key parameter for estimating the dimensions of earthquake ruptures, seismic moments, and earthquake magnitudes (e.g., Wells and Coppersmith, 1994; Wesnousky, 2008). Here, we use a high-resolution DEM (~5 m pixel size - data derived from the Greek Cadastre Agency), Google Earth imagery, and the ArcGIS software (version 10.6) to remap the traces of 53 known normal faults in the onshore area of metropolitan Athens (Fig. 5). All information related to these faults can be found in Table S1 that accompanies this work. These published faults (for references, see Table S1) provide the basis for the fault analysis presented here; yet, we have decided to revisit their lengths via analysis of a 5 m DEM. The reason for such an approach is that existing fault lengths derive from a combination of aerial photograph analysis (typically >1:10,000 scale), analysis of coarser DEMs (>20 m resolution), and field mapping (Lekkas *et al.*, 1992, 1995; Mariolakos and Fountoulis, 2000; Mariolakos *et al.*, 2001; Papanikolaou *et al.*, 2002; Ganas *et al.*, 2004, 2005;

Figure 5. (a) Map of fault traces as defined in this study. The number next to each fault corresponds to an entry in Table S1 in which all fault characteristics are summarized. Offshore faults derive from Papanikolaou *et al.* (1988, 1989), Leeder *et al.* (2002), Stefatos *et al.* (2002), Papanikolaou and Papanikolaou (2007), Sakellariou *et al.* (2007), and Charalampakis *et al.* (2014). (b) Fault map as in (a) with the relocated seismicity superimposed. The focal mechanism plots represent the four largest events derived from the National Observatory of Athens (NOA) moment tensor database (see Data and Resources). White dashes with letters in (a) and (b) delimit and provide direction of the depth cross sections illustrated in Figure 6. The color version of this figure is available only in the electronic edition.

Papanikolaou and Papanikolaou, 2007; Tsodoulos *et al.*, 2008; Sboras *et al.*, 2010; Grützner *et al.*, 2016; Deligiannakis *et al.*, 2018), techniques and tools that collectively provide fault throw resolution of ≥ 5 m (Begg and Mouslopoulou, 2010). Instead, by utilizing a 5 m DEM with a vertical resolution of 2 m (most fault scarps of ≥ 2 m are here resolved), we are able to increase the available fault trace information, especially along fault tips in which displacements are minimal. An example of a “revised” fault length is illustrated in Figure S7, in which the published length of the Leontari fault at ~13 km (Tsodoulos *et al.*, 2008) is now revised to 15.7 km on the 5 m DEM. The fault lengths that derive from our analysis are presented in Table S1 and are all within $\pm 20\%$ of the published lengths. Nevertheless, our revised fault lengths should also be considered as minimum values, as fault scarps of <2 m are not resolvable on the available DEM and also because fault scarps of any size may be partly or entirely modified by erosion, burial and/or anthropogenic factors. Topographic throw measurements for the onshore faults also derive from our DEM analysis.

In addition to retracing the length of 53 known active faults in the metropolitan region of Athens, we also identified a further five lineaments (faults 5, 6, 7, 9, and 10 in Table S1 and Fig. S8) which, on the basis of the geometry of their surface traces and vertical displacements, could be characterized as active normal faults (Fig. 5 and Fig. S8). These structures, which are all located within the eastern sector of Athens region, should be treated as potential rather than definite seismic sources (i.e., fieldwork is warranted to confirm their presence). Despite this, we have decided to include them in our analysis to draw the attention of the scientific community to their potential existence. It should be stressed that their inclusion has no impact on the first-order conclusions derived here, because their resolvable traces range from 2 to 8 km and their seismogenic potential is rather limited ($M_w < 6$; Table S1). Furthermore, in our analysis, we have also included the largest offshore faults (throw >300 m) located in the Saronikos Gulf (Papanikolaou *et al.*, 1988, 1989) and the largest active normal faults in the offshore eastern Corinth rift (Leeder *et al.*, 2002; Stefatos *et al.*, 2002; Sakellariou *et al.*, 2007; Charalampakis *et al.*, 2014). All attributes associated with these 22 offshore faults derive from previously published work (Papanikolaou *et al.*, 1988, 1989; Leeder *et al.*, 2002; Stefatos *et al.*, 2002; Papanikolaou and Papanikolaou, 2007; Sakellariou *et al.*, 2007; Charalampakis *et al.*, 2014) and can be found in Table S1.

For the purposes of this study, the individual traces that appear to be segments of a larger structure are treated as single faults and their length corresponds to the total length of their along-strike extent (e.g., faults 1, 12, 13, 22, 27, 29, 35, 41, 58, 59, 64, and 80). Furthermore, neighboring fault strands, which are located across distances of <5 km (Barka and Kadinsky-Cade, 1988; Wesnousky, 2006) and are possibly linked at depth (e.g., faults 20, 22, 29, 30, 37, 61, 65, 68, and 73), are considered here to form a single coherent fault system, and their length corresponds to the total along-strike extent of the fault system. For both cases, however, it remains possible that individual earthquakes rupture only partially these faults and fault systems (see the [Expected Moment Magnitudes](#) section).

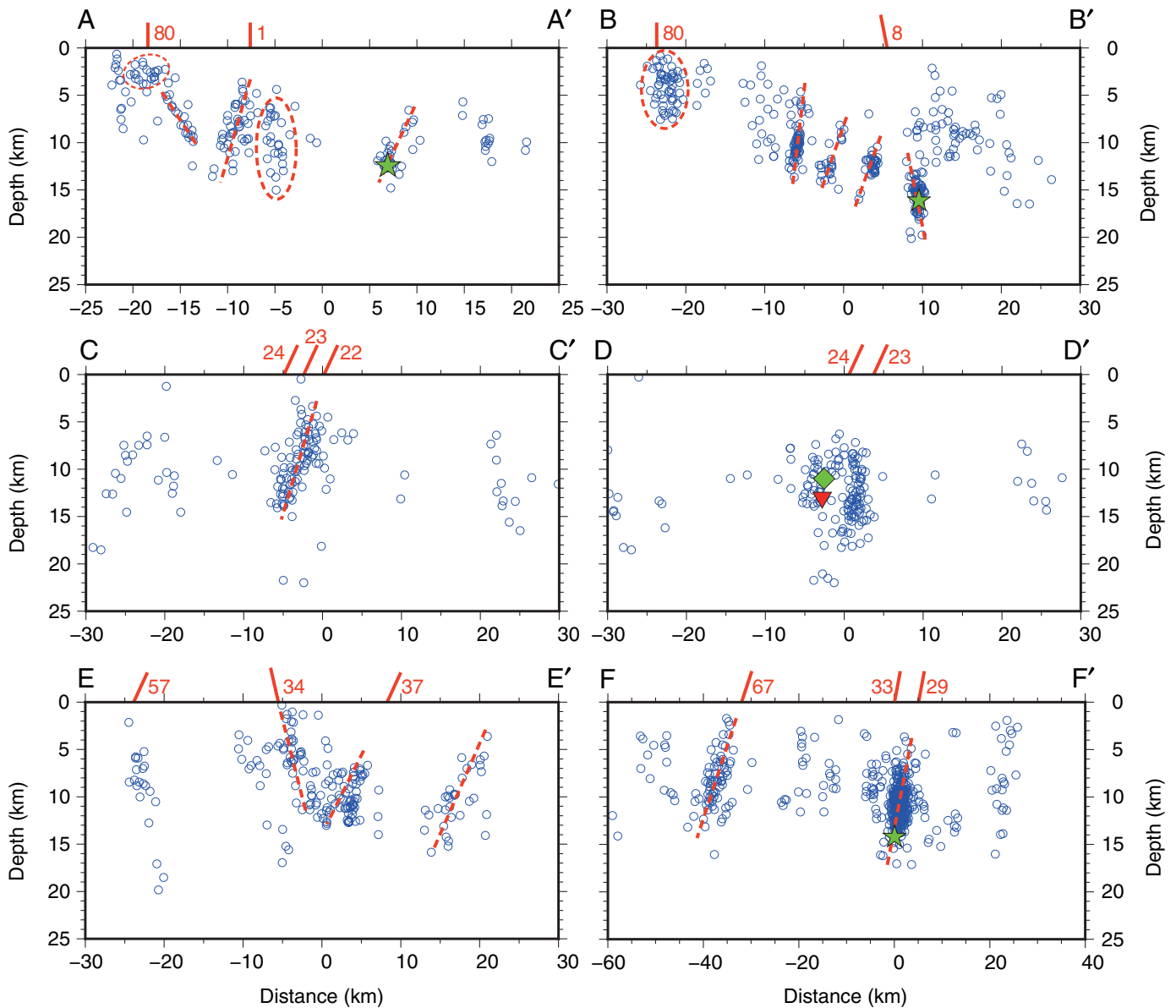
Collectively, we report on fault and earthquake parameters associated with 80 normal faults or fault systems. The majority ($>90\%$) of these faults traverse and displace limestone country, forming impressive scarps that can be traced for several kilometers (Fig. 5). A small number ($N = 5$) of these structures (faults 5, 6, 7, 9, and 21) are located within the basin of residential Athens and traverse alluvial materials to form subtle discontinuous scarps that may be partially buried or modified (Fig. 5). The 80 normal faults presented here are classified according to their activity as “faults with postglacial activity” and “faults without resolvable postglacial activity.” The postglacial activity on faults that displace limestone bedrock, which is the majority of the identified faults, is indicated by the presence of less-eroded and/or polished slip surfaces (often with striations) at the lower sections of their carbonate fault scarps. The notion that these sections of limestone scarps are formed

because of slip during large ($M_w > 6$) earthquakes since the last glaciation (~ 14 – 18 ka) is well established by cosmogenic dating of such scarps throughout the eastern Mediterranean (e.g., Mitchell *et al.*, 2001; Mozafari *et al.*, 2019), including Greece (Benedetti *et al.*, 2003; Mouslopoulou *et al.*, 2014; Mechernich *et al.*, 2018). For our study, we adopt the age of 16.5 ± 0.5 ka that derives from the dating of a carbonate fault scarp in Crete (Mouslopoulou *et al.*, 2014). The faults that exhibit unclear postglacial activity are faults that have either not ruptured the ground surface during the past ~ 16.5 ka or have produced surface displacements in the postglacial era that could not be resolved by the available datasets (they were either too small and/or were modified by erosion or sedimentation). These faults will be hereafter referred to as “less-active” faults; nevertheless, even if recent activity on them cannot be demonstrated, they should not be considered inactive, particularly if their orientation and dip direction are comparable to faults that are demonstrably active.

A total of 12 recorded normal faults are located within or east of Athens, another 45 are located west of Athens (including the Corinth rift), and 22 faults traverse the Saronikos Gulf and eastern Peloponnese. About 25% of the identified faults appear to have accommodated displacement during the last ~ 16 ka, whereas for the remaining faults, there is no evidence in support of postglacial activity. Nevertheless, these latter faults should not be considered inactive, because there are numerous examples of active faults globally (including Greece) that accommodate successive large earthquakes over timescales that exceed 16 ka (Mouslopoulou *et al.*, 2009, 2012; Hornblow *et al.*, 2014; Langridge *et al.*, 2016). This is also in accordance with the updated definition of active faults by the Greek Earthquake Protection and Planning Organization (EPPPO) that considers activity during the past 126 ka (EPPPO 102/21 June 2016). In the following section, we examine the spatial relationship between the relocated seismicity in the broader area of Athens and the distribution of active faults also including, whenever possible, focal mechanisms of events determined by NOA (Konstantinou *et al.*, 2010).

Active faulting and relocated seismicity

The relocated seismicity tends to be mostly localized along the eastern section of the Corinth rift, the Parnitha and Marathon regions, as well as offshore along the southwestern coastline of the Athens metropolitan area (Fig. 5b). The first-order observation that arises from the comparison between relocated seismicity and the distribution of faulting is that many of the faults that exhibit clear postglacial scarps (i.e., faults that have produced large earthquakes during the last ~ 16.5 ka) do not appear to accommodate significant microseismicity. This is in marked contrast to several faults with nonresolvable postglacial activity that are associated with clustered microseismicity. The most prominent example of the former case



relates to the normal faults close to Oropos (faults 14–17 in Fig. 5a), which are all associated with postglacial scarps and are likely responsible for the 1938 $M \sim 6$ Oropos earthquake (Grützner *et al.*, 2016; Deligiannakis *et al.*, 2018). Examples of the latter case include the Elefsis–Thriasio fault (fault 24), bounding the southern slope of Mt. Parnitha, the Dionysos–Penteli fault (fault 8) to the northeast of Athens, and the onshore and offshore faults along the eastern Corinth Gulf (Fig. 5a; Table S1). To better understand the spatial distribution of the relocated hypocenters with respect to the active faults, we constructed a number of depth cross sections perpendicular to the average strike of key earthquake clusters and faults (Fig. 5b) with a width that varies between 4 and 5 km on either side of the profiles. Figure 6 shows these depth cross sections, in which we have also indicated the apparent fault-plane dips, as defined by the relocated seismicity.

Figure 6. Depth cross sections corresponding to the profiles shown in Figure 5a,b. Dashed lines outline the main structural features of each cross section. The stars represent moderate magnitude events ($4 < M_w < 5$) that occurred in the study area during 2011–2018 (see [Active faulting and relocated seismicity](#) for more details). The diamond indicates the hypocenter of the 1999 Athens earthquake (from Papadimitriou *et al.*, 2002). The inverted triangle represents the hypocenter of the July 2019 moderate earthquake (obtained from NOAA catalog). The lines on top of each diagram indicate the location and dip direction of faults with clear surface expression that are intersected by each profile. The number next to each line corresponds to the fault numbers in Figure 5a and Table S1. Note that there is no information about the dip direction of fault 80, while cross section AA' cuts obliquely fault 1; hence, both of them are represented with vertical lines. The color version of this figure is available only in the electronic edition.

Cross-section AA' shows that seismicity offshore is quite shallow (< 5 km), whereas at larger depths, hypocenters form a plane that dips toward northeast. It is also possible to see

another cluster of microearthquakes on land that forms a plane that dips in the opposite direction to the previous fault, toward southwest. This cluster is located proximal to fault 1, and one could suggest that it reflects slip on this fault; however, a cross section perpendicular to fault 1 reveals no such relationship (Fig. S9). At the northeastern part of the cross section, a smaller fault plane can be defined that generated a moderate (M_w 4.1) earthquake on 4 June 2013 whose focal mechanism exhibits pure normal faulting with northwest–southeast strike. This small blind fault is situated near the edge of the runway of the Athens International Airport, a fact that possibly implies elevated seismic risk in the region. Along the cross section BB', the offshore seismicity remains shallow (1–7 km), although there is an even more pronounced deepening (down to ~20 km) of the hypocenters toward the northeast, compared to the cross-section AA'. Here, several tight clusters exist that form well-defined fault planes, which appear to dip toward southwest, except from the deepest of these clusters that have an apparent dip toward northeast (Fig. 6). This latter cluster, which seems to correlate with the Dionysos–Penteli fault (fault 8 in Fig. 5a), is also composed of the aftershocks of a moderate (M_w 4.1) earthquake that occurred on 15 January 2018 with a hypocentral depth of about 16 km (Figs. 5b and 6). If this event indeed nucleated along the Dionysos–Penteli fault, then it only ruptured the deeper section of this fault, because there are no aftershocks associated with the upper 10 km of the fault plane. Its focal mechanism shows pure normal faulting with northwest–southeast strike that agrees with the strike of the Dionysos–Penteli fault, but with a dip angle of 45° for both nodal planes that is less steep than the dip of the relocated cluster. This discrepancy has been also noted by Kaviris *et al.* (2018), and it could be attributed to the fact that for such small earthquakes aftershocks are rather limited in number and may not sample the fault plane adequately. The remaining seismicity that clusters along the profile BB' appears to occur on blind faults, because they do not correlate with any of the faults mapped at the ground surface.

In both AA' and BB' cross sections, there are clusters marked with dashed ellipses that do not seem to represent planar surfaces, but rather exhibit an elongated shape (Fig. 6). This difference cannot be attributed to the lack of hypocenter resolution, because vertical errors are ≤ 2 km and also neighboring clusters have a well-resolved planar shape. It is possible that these clusters represent microearthquake activity owing to the upward migration of fluids along one or more faults. This suggestion is supported by the fact that Saronikos Gulf has hosted significant volcanic activity from the Plio-Pleistocene till the Holocene (e.g., Pe-Piper and Piper, 2005) and extinct or presently dormant volcanoes (Sousaki and Methana) are situated nearby (Fig. 1a). Furthermore, available tomographic images in this area indicate low P -wave velocities (~3–4 km/s) in the depth range of 3.5–7 km (Drakatos *et al.*, 2005) and high V_p/V_s ratios (>1.8) between 10 and 20 km (Karakonstantis

et al., 2019). This seismicity, whether it is fluid-related or not, extends along the southwest coastline of residential Athens (Fig. 5) and defines a northwest–southeast-trending zone with a length of about 30 km. Despite its linearity, there is no unequivocal evidence for the presence of one or more active faults along this stretch of the coastline (Papanikolaou *et al.*, 1989). Increasing evidence, however, suggests that numerous large historic earthquakes (e.g., the 2010 M_w 7.1 Darfield and the 2016 M_w 7.8 Kaikōura earthquakes in New Zealand, the 2019 M_w 7.1 Ridgecrest earthquake sequence in the United States, etc.) have ruptured previously unknown faults, which were buried as a result of either fast sedimentation rates or long earthquake recurrence intervals (Mouslopoulou *et al.*, 2012, 2019; Hornblow *et al.*, 2014; Xu *et al.*, 2020). Thus, detailed submarine investigations and higher resolution geophysical imaging are required to decipher the existence of active faults along this area.

Cross sections CC' and DD' traverse an area that extends from the island of Salamina to the Parnitha region, where the 1999 Athens earthquake occurred, to Oropos region, terminating within the southern Evoikos Gulf (Fig. 5). The microseismicity here is concentrated along the foothills of Mt. Parnitha, clearly aligning with the parallel and closely spaced faults 22–24, with only few earthquakes located at either end of the profiles. In both profiles, at least one (and possible more) fault plane(s) may be defined by the clustered seismicity; interestingly, the fault-plane geometries appear to slightly differ along strike. In the easternmost profile CC', the indicated planes (faults 22 and 23) have an apparent dip toward southwest and are almost linear, whereas in cross section DD', the earthquakes extend deeper (down to 20 km) defining two parallel planes (faults 23 and 24). This apparent change in fault geometries can be rationalized if we examine Figure 5b more closely, in which profile CC' appears to sample mostly seismicity that occurs on the Fyli and Thrakomakedones faults (faults 22 and 23), whereas on profile DD' microseismicity is produced by the Elefsis–Thriasio and the Fyli faults (faults 23 and 24). For comparison, we plot along with the relocated events in profile DD', the hypocenter of the 1999 Athens earthquake (adopted from the study of Papadimitriou *et al.*, 2002) and the hypocenter (adopted from the catalog of NOA) of the most recent moderate magnitude (M_w 5.2) event that occurred on 19 July 2019. As it can be seen, the 1999 and 2019 events appear to be located in between two of the clusters that are defined by the relocated seismicity. This seismicity distribution is also consistent with rupture models of the 1999 earthquake (Baumont *et al.*, 2002, 2004; Roumelioti, Dreger, *et al.*, 2003) showing that the main slip patch extended from about 7 km down to a depth of 20 km.

Cross sections EE' and FF' extend from Saronikos Gulf to the basin of Thiva (Fig. 5b), traversing mainly faults that are elements of the Corinth rift with east–west strike. Some of these faults have exhibited recent significant activity (e.g., faults

44 and 29 that ruptured during the 1981 earthquake sequence) and others exhibited only little (if any) postglacial activity. For example, at the northern end of profile EE', seismicity defines a fault plane that dips toward the southwest and possibly relates to a series of normal faults in the Thiva basin that have accommodated little postglacial displacement (fault 37 in Fig. 5a). At the middle part of the cross section, we can observe a synthetic–antithetic fault structure along faults 34 and 37, even though some event clusters do not appear to follow the general trend of these two faults. A small cluster of events is located at the southern end of the cross section, near the Saronikos Gulf, and has an almost vertical orientation with hypocentral depths that range from 5 to about 12 km. Even though this cluster is spatially close to fault 57, there is a discrepancy between the apparent dip angle of the cluster and the southward dip of the fault plane. On the other hand, cross section FF' depicts two well-defined clusters with an apparent southward dip extending from a depth of less than 5 to about 15 km. The first cluster contains hundreds of events, some of them being aftershocks of a moderate 20 September 2013 M_w 4.3 earthquake that occurred offshore. The focal mechanism of this event exhibits normal faulting with nodal planes that strike northeast–southwest and seems more likely to be related to the Kapareli fault (fault 29, Fig. 5a) that generated the 4 March 1981 M_w 6.2 earthquake (Fig. 1b). The second large cluster in cross section FF' is located along the northern coastline of Argolida in Peloponnese and is possibly related to fault 67 that extends offshore and is associated with significant postglacial activity (Papanikolaou *et al.*, 1989). The rest of the events in cross section FF' do not exhibit any particular geometry, and it is difficult to associate them with any of the mapped faults.

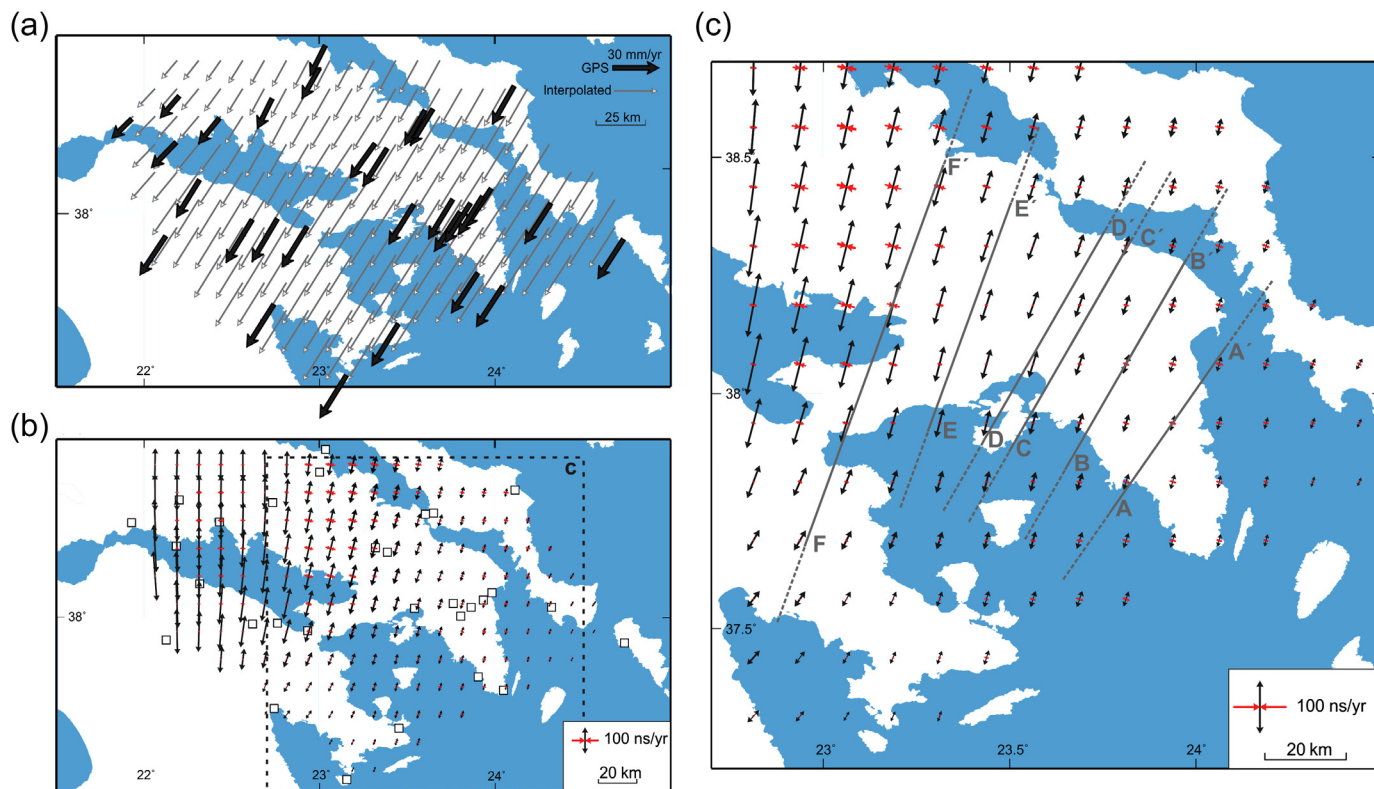
Active faulting and crustal deformation

The spatial distribution of strain rates in the metropolitan area of Athens complements the deformation patterns derived from the analysis of seismological and geological data by providing information on the elastic strain accumulation of the identified faults (i.e., the deformation accommodated within the Earth's crust in between large earthquakes). To derive regional strain rates for the broader metropolitan area of Athens, we used Global Positioning System (GPS) velocities recorded by 30 permanent GPS stations, which are located in northeast Peloponnese, Saronikos Gulf, eastern–central Greece, and Evia Island (Fig. 7a). The data collectively span a 10 yr time period (2003–2013) and derive from six international networks (HEPOS, METRICA, COMET and NTUA, CRL, NOANET, and EUREF). Further information on the data collection, processing, and analysis can be found in Chousianitis *et al.* (2015). Following the approach of weighted least squares (Menke, 1984; Shen *et al.*, 1996; Allmendinger *et al.*, 2012), we first established a regular 2D grid (with spacing 15 km × 15 km wide) over the entire region on which

predicted velocities were interpolated based on all stations of the network (Fig. 7a). Strain rates in the broader metropolitan area of Athens were calculated using these GPS-predicted velocities and are shown in Figure 7b,c. Uncertainties for each principal axis were estimated by calculating strain rates for 100 synthetic GPS datasets. The latter were generated using a Monte Carlo approach (Menke, 1984) and utilizing first-order data as the background dataset to which noise proportional to the observational uncertainties was added. Data suggest that there is an overall north-northeast increase in the amplitude of strain rates (Figs. 7b,c and 8a), from ~20 nstrain/yr in northeast Peloponnese to more than 40 nstrain/yr near the southern foothills of Mt. Parnitha. The latter area is the same area that hosted the 1999 Athens earthquake and the moderate magnitude (M_w 5.2) event on 19 July 2019.

To better explore the deformation gradients recorded within the study area, six individual strain rate and displacement rate profiles were calculated (Fig. 8). These profiles (see Fig. 7c for location) largely overlap with the six seismicity cross sections illustrated in Figure 5. Displacement rate gradients on these profiles range from ~1 mm/yr (profile AA') in eastern Athens to ~8 mm/yr (profile FF') across the eastern Corinth rift and Thiva region (Fig. 7c), with displacement rate variability (Fig. 8b) increasing with increasing strain rate (Fig. 8a). The overall positive slopes on all profiles in Figure 8b indicate extension, in agreement with the presence of active normal faulting in the study area (Fig. 5). Further examination of Figure 8b shows that, despite the uncertainties, significant (0.5–2.4 mm/yr) displacement rate changes occur close to where these profiles intersect known active or “less-active” faults (Fig. 8b), suggesting that elastic deformation may be localized along these faults. Although the density of the GPS values does not permit the unequivocal assignment of displacement rate gradients to individual faults, it does afford a first-order correlation, especially where geodetic rates can be compared to millennial displacement rates on individual faults. Table S2 compares geological and geodetic slip rates for a number of faults included in the profiles shown in Figure 8. The graphs in Figure 8b show the gradient in the geodetic displacement rate (black line) along each profile together with the locality of each fault (vertical lines with numbers). In circumstances for which only one fault spans the distance between two successive GPS values, a gradient is assigned to this fault (see “steps” in Fig. 8b). In circumstances where two or more faults intersect the profile between two successive GPS values, the gradient is assigned collectively to all faults (“slope” in Fig. 8b; see also Table S2).

Along profiles CC' and DD', for example, about 70% (~2 mm/yr) of the total slip-rate variability (~3 mm/yr) is accommodated over a distance of ~20 km across faults 22–24 (Mt. Parnitha region) and faults 15–18 (Oropos region; Fig. 8b). Geodetically derived displacement rates for these faults are comparable with fault displacement rates measured

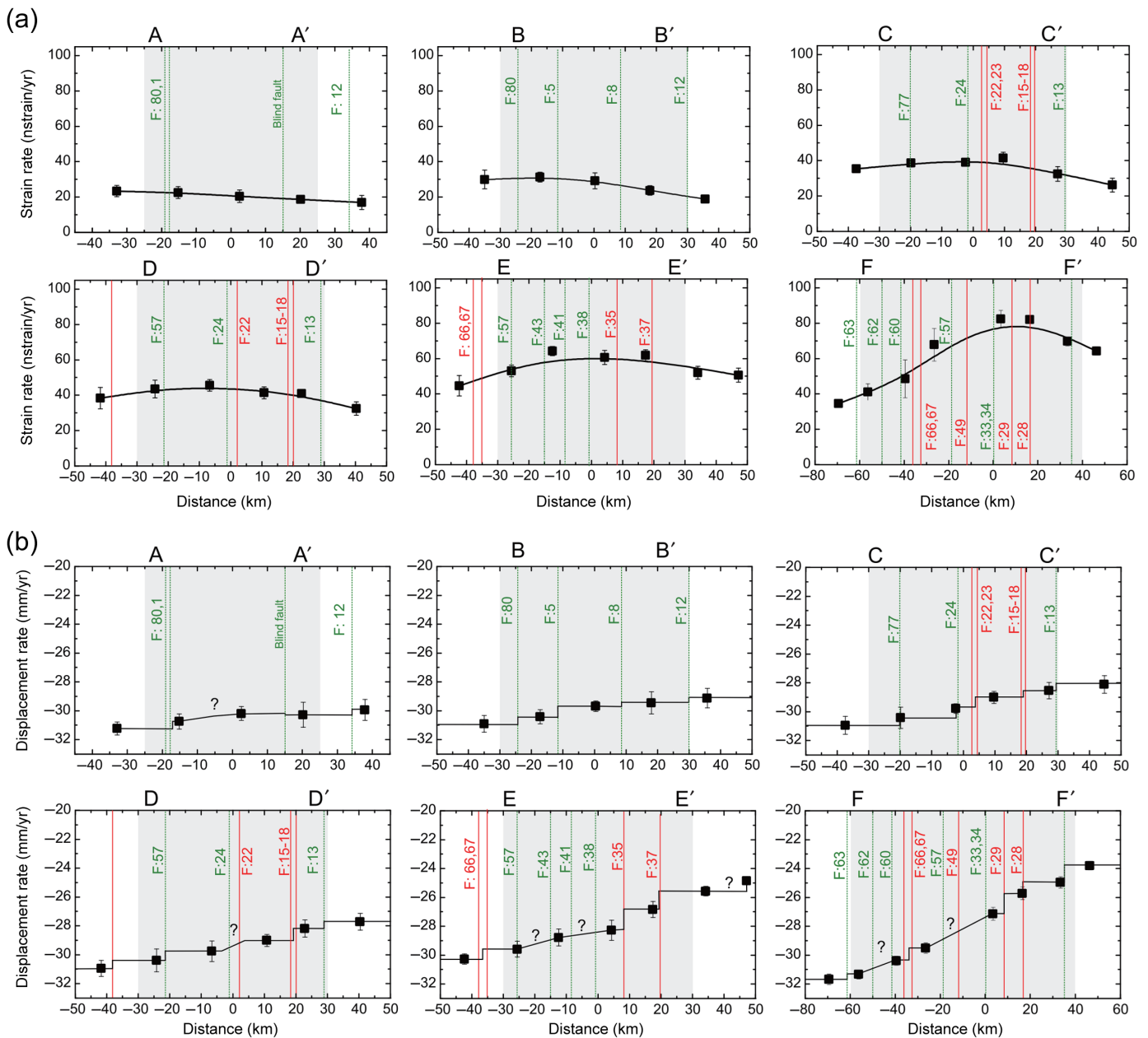


from their postglacial scarps over millennial timescales (see Table S2), reinforcing the notion that elastic deformation is localized along active faults and is converted into permanent deformation during large magnitude earthquakes (Nicol and Wallace, 2007). Our data also show that the “less-active” faults that intersect profiles C–C’ and D–D’ accommodate strain, with more pronounced being the Elefsis–Thriasio fault (fault 24), that appears to accommodate ~ 0.8 mm/yr.

Similarly, along profiles EE’ and FF’, the highest strain-rate values (Fig. 8a) and the steepest displacement rate gradients (Fig. 8b) occur in eastern Corinth rift and its onshore continuation, where the profiles intersect numerous known active faults (e.g., faults 28, 29, 35, 37, and 49). The geodetically derived displacement rate (2.4 mm/yr) across faults 33, 34, 49, and 57 on profile FF’ is broadly consistent with the geologically derived rate on fault 49 alone (~ 2.3 mm/yr), implying little or no strain accumulation on the three remaining faults (faults 33, 34, and 57; see Table S2), despite the fact that faults 33 and 34 host significant microseismicity (Fig. 6). By contrast, geodesy shows that significant displacement rate (~ 1 mm/yr) is accommodated across the “less-active” faults 43 and 57 on profile EE’ (Fig. 8b). Given that there is no requirement for significant elastic strain accumulation on fault 57 (see previously), the recorded strain may be stored on the Pateras fault (fault 43), a fault that today is considered to be inactive (Morewood and Roberts, 2002). Similarly, faults 60 and 62 in Peloponnese collectively accumulate ~ 1 mm/yr of elastic strain and are characterized by intense microseismicity

Figure 7. Summary of the geodetic observations: (a) Map of Global Positioning System (GPS) horizontal velocities with respect to the Eurasia plate indicated as black arrows, whereas gray arrows indicate 2D interpolated velocities. (b) Strain-rate map derived from GPS data. Arrows correspond to first (extensional) and second (compressional) principal axis. Empty squares indicate location of GPS stations (see also Chousianitis *et al.*, 2015). Dashed rectangle marks the area shown in (c). (c) Strain-rate map in the broader area of metropolitan Athens. Gray letters correspond to the strain-rate and displacement-rate profiles illustrated in Figure 8. The color version of this figure is available only in the electronic edition.

(Fig. 6), although they lack postglacial activity. Comparison between geodesy and geology on profile F–F’ for the Kaparelli fault (fault 29) suggests that outcrop geology may have underestimated its displacement rate by a factor of five (1.5 vs. 0.3 mm/yr). Significant strain (~ 0.8 mm/yr) may also be accumulated across the Leontari fault (fault 28), which is possibly the fault responsible for the 1893 M_w 6.7 Thiva earthquake (Ambraseys and Jackson, 1990; Goldsworthy and Jackson, 2000; Goldsworthy *et al.*, 2002). Faults 35 and 37 collectively accommodate about 3 mm/yr of geodetically derived displacement rate, although very little is known about their postglacial activity. On the contrary, the majority of the faults identified in the eastern part of Athens are characterized by low strain and displacement rate gradients (Figs. 7 and 8), indicating that this part of the study area has limited earthquake potential.



EXPECTED MOMENT MAGNITUDES

The brittle part of the crust, usually referred to as the seismogenic layer, defines the limit of rupture extent during large earthquakes and is an important parameter when assessing magnitudes of expected earthquakes in an area. To calculate expected magnitudes for the faults in our study area, first, we estimate the thickness of the seismogenic layer by utilizing the relocated hypocenters. To achieve this, the study area was divided into three sectors, two of them covering the area east and west of the detachment (Fig. 1b), and a third one containing the Saronikos Gulf and the northeast coastline of Peloponnese. This division is based on the different lithology on either side of the detachment (alpine sedimentary formations vs. exhumed metamorphic rocks; Papanikolaou and Papanikolaou, 2007; Krohe *et al.*, 2010) and the fact that

Figure 8. (a) Strain rate (nstrain/yr) transects along the six profiles indicated in Figure 7c. Gray shading corresponds to the solid section of the profiles illustrated in Figure 7c and is directly comparable to the seismicity depth cross sections presented in Figures 5b and 6. Solid black lines represent the average distribution of strain rates along each profile. Locations of representative faults along each profile are also included. For fault numbers, refer to Figure 5a and Table S1. (b) Similar to (a) with displacement rates (mm/yr) shown on the y axes. Stepped lines plotted near known active faults assume that displacement rate changes between successive points are elastically accommodated on these faults. Question marks denote uncertainties in the exact location of the stepped profile. Two-sigma uncertainties are also shown. For comparison between the geodetically derived GPS rates and fault displacement rates, see Table S2. The color version of this figure is available only in the electronic edition.

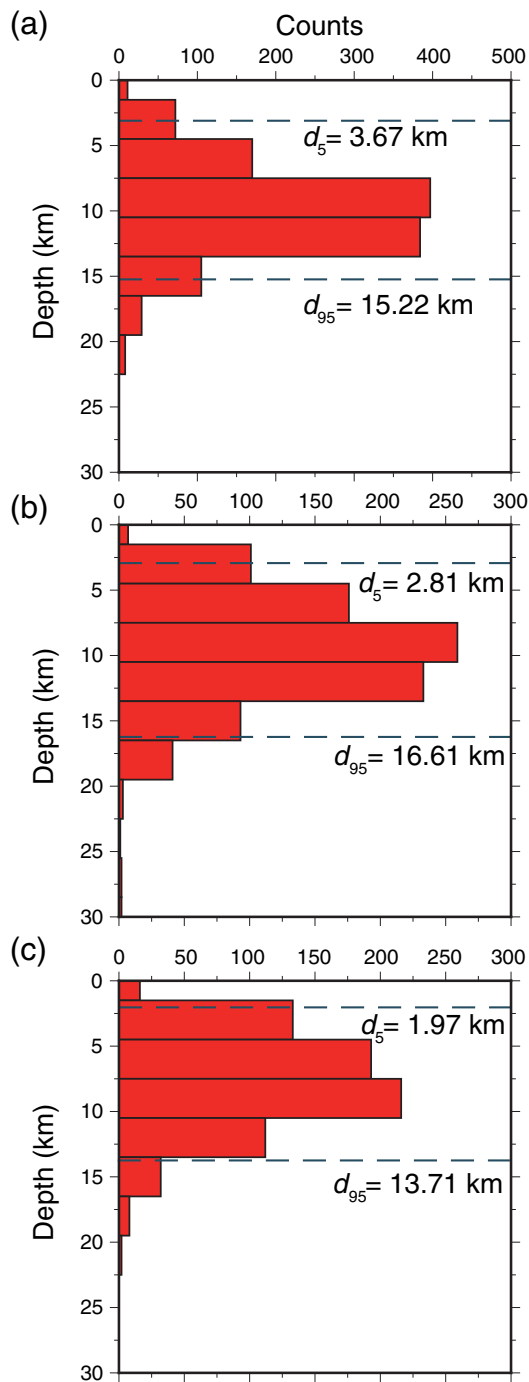


Figure 9. Histograms depicting the distribution of hypocentral depth for the relocated events for (a) the sector west of the detachment, (b) east of the detachment, and (c) Saronikos Gulf. The 5th and 95th percentiles in each plot are given by the symbols d_5 and d_{95} , respectively. Bin size is in all cases 3 km, which is proportional to the vertical uncertainty of the relative locations. The color version of this figure is available only in the electronic edition.

Saronikos has hosted significant volcanism and geothermal activity from the Plio-Pleistocene until now, leading to elevated heat-flow values (80–100 mW/m², Fytikas and Kolios, 1979).

The hypocenters for each of these sectors were then used to construct histograms of their depth distribution with a bin size of 3.0 km (Fig. 9), which is proportional to the range of their average vertical uncertainty (1.15 ± 1.97 km). The 5th and 95th percentiles of each distribution were then used as the onset and cutoff depth of seismogenesis for each sector. As it can be seen in Figure 9, two of the sectors (west and Saronikos) exhibit almost the same values of thickness for the seismogenic layer that range from 11.7 to 11.5 km, whereas the eastern sector exhibits a larger value of 13.8 km.

We calculated the expected earthquake magnitude along each of the delineated faults using the empirical relationships of Konstantinou (2014) that were calibrated for moment magnitudes and rupture areas of events occurring in the Mediterranean region. These relationships can be described as

$$M_w = \log A + 3.82, \quad \text{when } A \leq 251 \text{ km}^2,$$

$$M_w = (4/3) \log A + 3.07, \quad \text{when } A > 251 \text{ km}^2,$$

in which A signifies the rupture area in square kilometers. Table S1 lists the length L , width W , and dip angle for each of the faults included in this study. Rupture area of each fault can be subsequently calculated as the product $L \times W$, in which the width W is equal to the seismogenic layer thickness divided by the sine of the dip angle. As discussed in the Identification and Classification of Faults section, in circumstances in which faults include individual segments and/or form a fault system, their fault length (L) corresponds to their total along-strike extent. However, it remains possible that individual earthquakes would rupture only a section of these faults and fault systems. Using these relationships, we were able to calculate expected moment magnitudes for all mapped faults (Fig. 5a).

In Figure 10, we present only those faults that are capable of generating earthquakes with magnitude 6.0 or larger. (Table S1 contains expected magnitudes for all faults.) As mentioned previously, several of the faults that are situated to the west of the detachment have accommodated large earthquakes during the past ~16 ka (Fig. 5a) but exhibited little or no microseismicity during the past 8 yr (faults 18, 15, 29, 35, 58, 59, 65, 66, and 68 in Figs. 5b and 10). This observation, coupled with evidence that elastic strain is being currently stored in these structures (Fig. 8 and Table S2), suggests that these faults may be “locked” and under a regime of velocity strengthening (Moreno *et al.*, 2014). Unlike to what has been observed in the west, in the east, seismicity occurs mainly along small unresolved blind faults (Fig. 5b), whereas along the faults with surface expression, there is no significant microseismicity. Therefore, it is likely that in the future this area may generate only moderate-sized earthquakes ($M_w < 5$), perhaps with the exception of the Dionysos–Penteli fault (fault 8) whose expected moment magnitude is larger (~6.2).

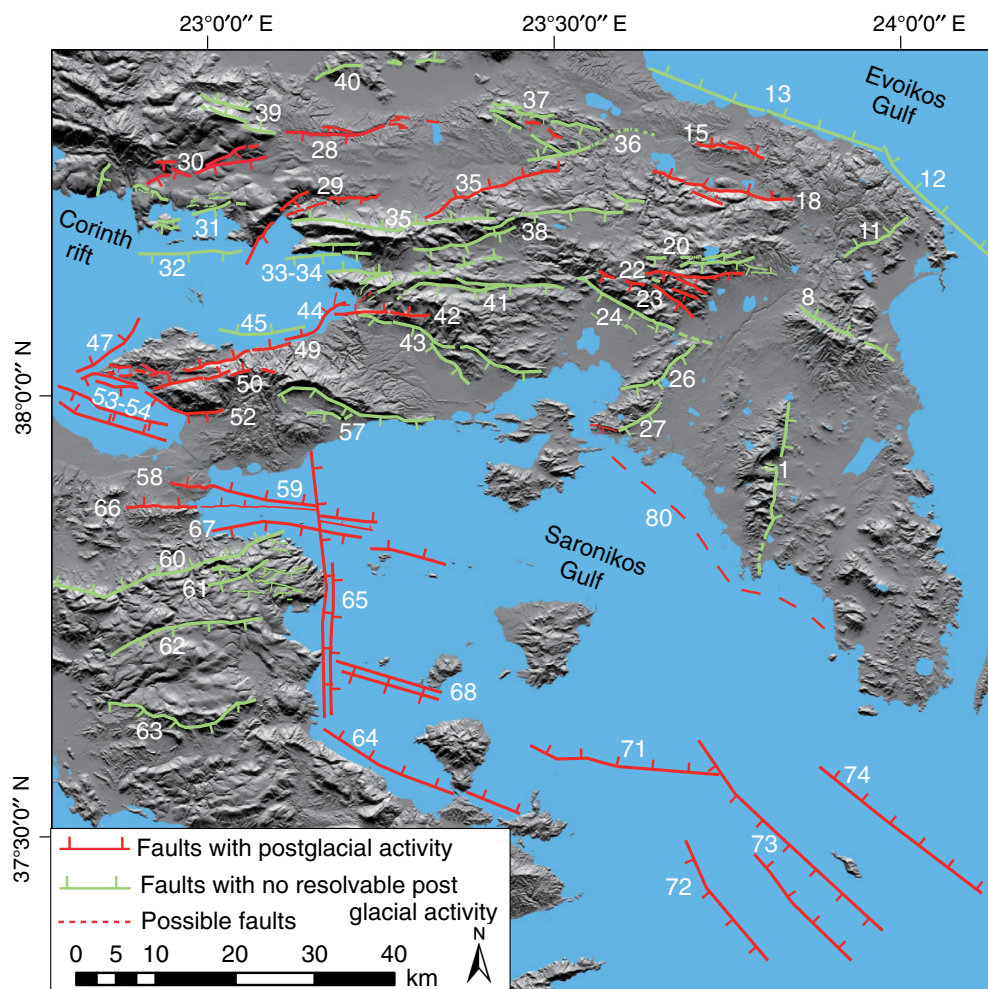


Figure 10. Fault map illustrating which of the identified structures can generate earthquakes with moment magnitude $M_w \geq 6$. The number next to each fault corresponds to an entry in Table S1 in which all fault characteristics are summarized. The color version of this figure is available only in the electronic edition.

CONCLUSIONS

The existence of active faults near a major city constitutes a significant hazard for the life and property of its inhabitants as well as for its public infrastructure. Large earthquakes generated by these faults may be very destructive, owing to a combination of complex rupture, directivity, and local site effects. The city of Athens stands out as an example of a modern metropolis that experienced such a large (M_w 6) earthquake in 1999, sustaining heavy damage and casualties. In this study, we tried to highlight the importance of combining different datasets and timescales in assessing the seismic hazard posed to a modern metropolis. Specifically, we have systematically mapped the seismicity distribution within a radius of about 50 km from Athens and explored its relationship with the patterns of active faulting and interseismic strain accumulation. A summary of the main conclusions of this work is the following:

1. In the period 2011–2018, a total of 4722 earthquakes were recorded in the area around Athens with the majority

having local magnitudes smaller than 3.0 and only four events reaching magnitudes between 4.1 and 4.3. The good station coverage around Athens resulted in uncertainties for absolute locations that are on average 2.2 km horizontally and 3.2 km vertically. This was not the case for the offshore area of Saronikos Gulf, where the lack of nearby stations increased these uncertainties to a value of 5 km or larger. This is unfortunate, because this area is well known for its high-seismicity levels (Makris *et al.*, 2004). The installation of additional stations at the islands of Saronikos and at the coast of Peloponnese would significantly increase the quality of absolute locations and enhance our knowledge on the existence of active faults offshore.

2. Precise relative locations of 2666 events were obtained with horizontal and vertical uncertainties that did not exceed 1 and 2 km, respectively.

Microseismicity patterns were compared with active fault patterns derived from analysis of a 5 m DEM and with strain rates derived from interseismic GPS velocities. Comparison shows that microseismicity is mostly located along faults that have exhibited little or no postglacial activity (~ 16 ka), whereas most faults that were active in the past ~ 16 ka (and even historically) do not appear to host significant microseismicity. Nevertheless, GPS data indicate that both types of faults (active and “less-active”) currently accumulate elastic deformation that ranges, on individual faults, from ~ 0.5 to ~ 2.4 mm/yr. These values, where available, are broadly consistent with displacement rate measurements that derive from outcrop geology, suggesting that elastic deformation will be likely converted into permanent deformation in the future owing to large earthquakes.

3. Strain rates increase from 20 nstrain/yr in the Saronikos Gulf to about 40 nstrain/yr at Mt. Parnitha, very close to the Athens metropolitan area. This increase coincides

with significant microseismic activity along well-defined faults at the southern foothills of Mt. Parnitha, where the two large and moderate earthquakes occurred in 1999 and 2019, respectively.

4. The detachment that traverses Athens in a northeast-southwest orientation separates the sedimentary (west) from the metamorphic rocks (east) and may represent a significant boundary to earthquake rupture propagation. This is because west of the detachment there is extensive active faulting and associated seismicity as opposed to the seismically “quiet” area east of the detachment. The seismogenic layer thickness varies from about 11 km west of the detachment and in Saronikos Gulf, to about 14 km east of the detachment. This might seem to suggest that larger earthquakes can potentially occur in the eastern area; however, only small blind faults could be detected there by our study.
5. By taking into account the recorded thickness of the seismogenic layer for each region, we estimated expected earthquake magnitudes along the identified faults using empirical relationships that connect moment magnitude with rupture area. The results show that >50% of the mapped faults ($N = 54$) are capable of generating earthquakes with moment magnitudes between 6.0 and 6.6. Of particular concern are the faults to the north of Athens (near Oropos) that lack significant microseismicity during the past 8 yr, while they have been accumulating elastic strain at rates of up to 0.8 ± 0.4 mm/yr, as well as faults with no postglacial activity west of the detachment that currently accommodate significant (>0.5 mm/yr) elastic deformation and associated microseismicity. Thus, our study shows that in addition to the known active fault sources, the metropolitan area of Athens may accommodate additional seismic sources. These faults, despite the fact that they are characterized by long recurrence intervals, are mostly associated with intense microseismicity and elastic strain accumulation, signifying the need for future investigations on their seismogenic potential.

DATA AND RESOURCES

The waveform data that were used in this study for picking P and S phases are freely available for download from National Observatory of Athens (NOA), European Integrated Data Archive (EIDA) archives under the network code Hellenic Unified Seismic Network (HUSN) (<http://eida.gein.noa.gr/>, last accessed January 2019). Initial locations and local magnitudes were adopted from the revised events database of NOA available at <http://bbnet.gein.noa.gr/HL/databases/database> (last accessed September 2019). Moment tensor solutions were adopted from the revised moment tensor database of NOA at <http://bbnet.gein.noa.gr/HL/seismicity/mts/revised-moment-tensors> (last accessed January 2020). The geodetic data of NOA are freely available for download from <http://geodesy.gein.noa.gr:8000/nginfo/data/> (last accessed January 2020). The Global Centroid Moment Tensor (Global CMT) Project database was searched using www.globalcmt.org/

[CMTsearch.html](http://www.globalcmt.org/) (last accessed August 2019). Google Earth imagery was last accessed in August 2019. The digital elevation model (DEM) used in this study was provided by the Greek Cadastre Agency and it is not publicly available. The supplemental material that accompanies this work contains nine figures (Figs. S1–S9) and two tables (Tables S1 and S2) in Excel format that describe attributes of the 80 faults shown in the figures and discussed in the article.

ACKNOWLEDGMENTS

Kostas I. Konstantinou would like to thank the Ministry Of Science and Technology of Taiwan (MOST) for the financial support of this study in the form of an awarded grant. Vasiliki Mouslopoulou acknowledges support from an internal National Observatory of Athens (NOA) Fellowship, whereas Vasso Saltogianni was supported by an Alexander Von Humboldt Fellowship. The authors are grateful to the staff of the Institute of Geodynamics (NOA) for data archiving and processing and to the Greek Cadastre Agency for providing the high-resolution digital elevation model (DEM) for the active fault analysis. John Begg (GNS Science) and Dimitrios Sakellariou (ELKETHE) are thanked for helpful discussions on onshore and offshore active faulting, respectively. The authors would like to thank Yann Klinger for handling their article and two anonymous reviewers for their constructive criticism that improved this article.

REFERENCES

- Aki, K. (1965). Maximum likelihood estimate of b in the formula $\log N = a - bM$ and its confidence limits, *Bull. Earthq. Res. Inst. Tokyo Univ.* **43**, 237–239.
- Allmendinger, R. W., N. Cardozo, and D. M. Fisher (2012). *Structural Geology Algorithms, Vectors and Tensors*, Cambridge University Press, Cambridge, United Kingdom.
- Ambraseys, N., and I. N. Psycharis (2012). Assessment of the long-term seismicity of Athens from two classical columns, *Bull. Earthq. Eng.* **10**, 1635–1666, doi: [10.1007/s10518-012-9388-1](https://doi.org/10.1007/s10518-012-9388-1).
- Ambraseys, N. N., and J. A. Jackson (1990). Seismicity and associated strain of central Greece between 1890 and 1988, *Geophys. J. Int.* **101**, 663–708.
- Barka, A. A., and K. Kadinsky-Cade (1988). Strike-slip fault geometry in Turkey and its influence on earthquake rupture, *Tectonics* **7**, 663–684.
- Baumont, D., F. Courboulex, O. Scotti, N. Melis, and G. Stavrakakis (2002). Slip distribution of the M_w 5.9, 1999 Athens earthquake inverted from regional seismological data, *Geophys. Res. Lett.* **29**, 1720, doi: [10.1029/2001GL014261](https://doi.org/10.1029/2001GL014261).
- Baumont, D., O. Scotti, F. Courboulex, and N. Melis (2004). Complex kinematic rupture of the M_w 5.9, 1999 Athens earthquake as revealed by the joint inversion of regional seismological and SAR data, *Geophys. J. Int.* **158**, 1078–1087, doi: [10.1111/j.1365-246X.2004.02374.x](https://doi.org/10.1111/j.1365-246X.2004.02374.x).
- Begg, J. G., and V. Mouslopoulou (2010). Analysis of late Holocene faulting within an active rift using lidar, Taupo rift, New Zealand, *J. Volcanol. Geoth. Res.* **190**, 152–167.
- Benedetti, L., R. Finkel, G. King, R. Armijo, D. Papanastassiou, F. J. Ryerson, F. Flerit, D. Farber, and G. Stavrakakis (2003). Motion on the Kaparelli fault (Greece) prior to the 1981 earthquake sequence determined from ^{36}Cl cosmogenic dating, *Terra Nova* **15**, 118–124.

- Biasi, G. P., and S. G. Wesnousky (2017). Bends and ends of surface ruptures, *Bull. Seismol. Soc. Am.* **107**, 2543–2560.
- Charalampakis, M., V. Lykousis, D. Sakellariou, G. Papatheodorou, and G. Ferentinos (2014). The tectono-sedimentary evolution of the Lechaion Gulf, the south eastern branch of the Corinth graben, Greece, *Mar. Geol.* **351**, 58–75, doi: [10.1016/j.margeo.2014.03.014](https://doi.org/10.1016/j.margeo.2014.03.014).
- Chousianitis, K., A. Ganas, and C. P. Evangelidis (2015). Strain and rotation rate patterns of the mainland Greece from continuous GPS data and comparison between seismic and geodetic moment release, *J. Geophys. Res.* **120**, doi: [10.1002/2014JB011762](https://doi.org/10.1002/2014JB011762).
- D'Alessandro, A., D. Papanastassiou, and I. Baskoutas (2011). Hellenic Unified Seismic Network: An evaluation of its performance through SNES method, *Geophys. J. Int.* **185**, 1417–1430, doi: [10.1111/j.1365-246X.2011.05018.x](https://doi.org/10.1111/j.1365-246X.2011.05018.x).
- Deligiannakis, G., I. D. Papanikolaou, and G. Roberts (2018). Fault specific GIS based seismic hazard maps for the Attica region, Greece, *Geomorphology* **306**, 264–282, doi: [10.1016/j.geomorph.2016.12.005](https://doi.org/10.1016/j.geomorph.2016.12.005).
- Drakatos, G., V. Karastathis, J. Makris, J. Papoulia, and G. Stavrakakis (2005). 3D crustal structure in the neotectonic basin of the Gulf of Saronikos (Greece), *Tectonophysics* **400**, 55–65, doi: [10.1016/j.tecto.2005.02.004](https://doi.org/10.1016/j.tecto.2005.02.004).
- Drakatos, G., N. Melis, D. Papanastasiou, V. Karastathis, G. A. Papadopoulos, and G. Stavrakakis (2002). 3-D crustal velocity structure from inversion of local earthquake data in Attiki (central Greece) region, *Nat. Hazards* **27**, 1–14.
- Font, Y., H. Kao, S. Lallemand, C. S. Liu, and L. Y. Chiao (2004). Hypocenter determination offshore of eastern Taiwan using the maximum intersection method, *Geophys. J. Int.* **158**, 655–675.
- Fytikas, M. D., and N. P. Kolios (1979). Preliminary heat flow map of Greece, in *Terrestrial Heat Flow in Europe*, Springer, Berlin, Heidelberg, Germany, 197–205.
- Ganas, A., S. Pavlides, and V. Karastathis (2005). DEM-based morphometry of range-front escarpments in Attica, central Greece, and its relation to fault slip rates, *Geomorphology* **65**, 301–319.
- Ganas, A., S. B. Pavlides, S. Sboras, S. Valkaniotis, S. Papaioannou, G. A. Alexandris, A. Plessa, and G. A. Papadopoulos (2004). Active fault geometry and kinematics in Parnitha Mountain, Attica, Greece, *J. Struct. Geol.* **26**, 2103–2118.
- Goldsworthy, M., and J. Jackson (2000). Active normal fault evolution in Greece revealed by geomorphology and drainage patterns, *J. Geol. Soc. Lond.* **157**, 967–981.
- Goldsworthy, M., J. Jackson, and J. Haines (2002). The continuity of active faults systems in Greece, *Geophys. J. Int.* **148**, 596–618.
- Gomberg, J. S., K. M. Shedlock, and S. W. Roecker (1990). The effect of S-wave arrival times on the accuracy of hypocentre estimation, *Bull. Seismol. Soc. Am.* **80**, 1605–1628.
- Grützner, C., S. Schneiderwind, I. Papanikolaou, G. Deligiannakis, A. Pallikarakis, and K. Reicherter (2016). New constraints on extensional tectonics and seismic hazard in northern Attica, Greece—The case of the Milesi fault, *Geophys. J. Int.* **204**, 180–199, doi: [10.1093/gji/ggv443](https://doi.org/10.1093/gji/ggv443).
- Hatzfeld, D., J. Martinod, G. Bastet, and P. Gautier (1997). An analog experiment for the Aegean to describe the contribution of gravitational potential energy, *J. Geophys. Res.* **102**, 649–659.
- Hornblow, S., M. Quigley, A. Nicol, R. Van Dissen, and N. Wang (2014). Paleoseismology of the 2010 M_w 7.1 Darfield (Canterbury) earthquake source, Greendale Fault, New Zealand, *Tectonophysics* **637**, 178–190.
- Karakonstantis, A., P. Papadimitriou, C. Millas, I. Spingos, I. Fountoulakis, and G. Kaviris (2019). Tomographic imaging of the NW edge of the Hellenic volcanic arc, *J. Seismol.* **23**, 995–1016, doi: [10.1007/s10950-019-09849-8](https://doi.org/10.1007/s10950-019-09849-8).
- Kaviris, G., I. Spingos, C. Millas, V. Kapetanidis, I. Fountoulakis, P. Papadimitriou, N. Voulgaris, and G. Drakatos (2018). Effects of the January 2018 seismic sequence on shear-wave splitting in the upper crust of Marathon (NE Attica, Greece), *Phys. Earth Planet. In.* **285**, 45–58, doi: [10.1016/j.pepi.2018.10.007](https://doi.org/10.1016/j.pepi.2018.10.007).
- Kissling, E. (1995). *Program VELEST User's Guide—Short Introduction*, Institute of Geophysics, ETH Zurich, Zurich, Switzerland.
- Kissling, E., W. L. Ellsworth, D. Eberhart-Phillips, and U. Kradolfer (1994). Initial reference models in local earthquake tomography, *J. Geophys. Res.* **99**, 19,635–19,646.
- Konstantinou, K. I. (2014). Moment magnitude-rupture area scaling and stress-drop variations for earthquakes in the Mediterranean region, *Bull. Seismol. Soc. Am.* **104**, 2378–2386, doi: [10.1785/0120140062](https://doi.org/10.1785/0120140062).
- Konstantinou, K. I., I. S. Kalogeras, N. S. Melis, M. C. Kourouzidis, and G. N. Stavrakakis (2006). The 8 January 2006 earthquake (M_w 6.7) offshore Kythira Island, southern Greece: Seismological, strong-motion and macroseismic observations of an intermediate-depth event, *Seismol. Res. Lett.* **77**, 544–553.
- Konstantinou, K. I., N. S. Melis, and K. Boukouras (2010). Routine regional moment tensor inversion for earthquakes in the Greek region: The National Observatory of Athens (NOA) database (2001–2006), *Seismol. Res. Lett.* **81**, 750–760, doi: [10.1785/gssrl.81.5.750](https://doi.org/10.1785/gssrl.81.5.750).
- Konstantinou, K. I., V. Mouslopoulou, W.-T. Liang, O. Heidbach, O. Oncken, and J. Suppe (2016). Present-day crustal stress field in Greece inferred from regional-scale damped inversion of earthquake focal mechanisms, *J. Geophys. Res.* **121**, doi: [10.1002/2016JB013272](https://doi.org/10.1002/2016JB013272).
- Krohe, A., E. Mposkos, A. Diamantopoulos, and G. Kaouras (2010). Formation and mountain ranges in Attica (Greece): The role of Miocene to recent low-angle normal detachment faults, *Earth Sci. Rev.* **98**, 81–104, doi: [10.1016/j.earscirev.2009.10.005](https://doi.org/10.1016/j.earscirev.2009.10.005).
- Langridge, R. M., W. F. Ries, N. J. Litchfield, P. Villamor, R. J. Van Dissen, D. J. A. Barrell, M. S. Rattenbury, D. W. Heron, S. Haubrock, D. B. Townsend, et al. (2016). The New Zealand active faults database, *New Zeal. J. Geol. Geophys.* **59**, 86–96.
- Leeder, M. R., R. E. Collier, L. H. Abdul Aziz, M. Trout, G. Ferentinos, G. Papatheodorou, and E. Lyberis (2002). Tectono-sedimentary processes along an active marine/lacustrine margin: Alkyonides Gulf, E. Gulf of Corinth, Greece, *Basin Res.* **14**, 25–41.
- Lekkas, E. (2001). The Athens earthquake (7 September 1999): Intensity distribution and controlling factors, *Eng. Geol.* **59**, 297–311.
- Lekkas, E., D. Papanikolaou, and I. Fountoulis (1992). Neotectonic Map of Greece, Scale 1:100,000, Department of Dynamic, Tectonic and Applied Geology, University of Athens, Athens, Greece.
- Lekkas, E., D. Papanikolaou, S. Lozios, I. Papoulia, and S. Vasilopoulou (1995). *Neotectonic Map of Eastern Attica*, Department of Dynamic, Tectonic and Applied Geology

- (University of Athens) & Prefecture of Eastern Attica, Athens, Greece.
- Lomax, A., and A. Curtis (2001). Fast, probabilistic earthquake location in 3D models using Oct-Tree importance sampling, *Geophys. Res. Abstr.* **3**, 955.
- Lomax, A., A. Michelini, and A. Curtis (2009). Earthquake location, direct, global-search methods, in *Complexity in Encyclopedia of Complexity and System Science, Part 5*, R. A. Meyers (Editor), Springer, New York, New York, 2449–2473, doi: [10.1007/978-0-387-30440-3](https://doi.org/10.1007/978-0-387-30440-3).
- Lomax, A., J. Virieux, P. Volant, and C. Berge-Thierry (2000). Probabilistic earthquake location in 3D and layered models, in *Advances in Seismic Event Location*, C. H. Thurber and N. Rabinowitz (Editors), Kluwer, Amsterdam, The Netherlands, 101–134.
- Makris, J., J. Papoulia, and G. Drakatos (2004). Tectonic deformation and microseismicity of the Saronikos Gulf, Greece, *Bull. Seismol. Soc. Am.* **94**, 920–929.
- Maleki, V., Z. Hossein Shomali, M. R. Hatami, M. Pakzad, and A. Lomax (2013). Earthquake relocation in the central Alborz region of Iran using a nonlinear probabilistic method, *J. Seismol.* **17**, 615–628, doi: [10.1007/s10950-012-9342-3](https://doi.org/10.1007/s10950-012-9342-3).
- Mariolagos, I., and I. Fountoulis (2000). The Athens earthquake September 7, 1999 neotectonic regime and geodynamic phenomena, *Ann. Géol. Pays Hellén.* **38**, no. B, 165–174.
- Mariolagos, I., I. Fountoulis, and D. Theocharis (2001). Neotectonic structure and evolution of the Salamina Island, *Bull. Geol. Soc. Greece, Proc. of the 9th International Congress*, Athens, Greece, September 2001, Vol. XXIV/1, 165–173.
- Martinod, J., D. Hatzfeld, J.-P. Brun, J.-P. Davy, and P. Gautier (2000). Continental collision, gravity spreading, and kinematics of Aegea and Anatolia, *Tectonics* **19**, 290–299.
- Mechernich, S., S. Schneiderwind, J. Mason, I. D. Papanikolaou, G. Deligiannakis, A. Palikarakis, S. A. Binnie, T. J. Dunai, and K. Reicherter (2018). The seismic history of the Pisias fault (eastern Corinth rift, Greece) from fault plane weathering features and cosmogenic ³⁶Cl Dating, *J. Geophys. Res.* **123**, 4266–4284.
- Meijer, P. T., and M. J. R. Wortel (1997). Present-day dynamics of the Aegean region: A model analysis of the horizontal pattern of stress and deformation, *Tectonics* **16**, 879–895.
- Menke, W. (1984). *Geophysical Data Analysis: Discrete Inverse Theory*, Academic Press, Orlando, Florida.
- Mitchell, S. G., A. Matmon, P. R. Bierman, Y. Enzel, M. Caffee, and D. Rizzo (2001). Displacement history of a limestone normal fault scarp, northern Israel, from cosmogenic ³⁶Cl, *J. Geophys. Res.* **106**, no. B106, 4247–4264.
- Moreno, M., C. Haberland, O. Oncken, A. Rietbrock, S. Angiboust, and O. Heidbach (2014). Locking of the Chile subduction zone controlled by fluid pressure before the 2010 earthquake, *Nature Geosci.* **7**, no. 4, 292–296, doi: [10.1038/ngeo2102](https://doi.org/10.1038/ngeo2102).
- Morewood, N. C., and G. P. Roberts (2002). Surface observations of active normal fault propagation: Implications for growth, *J. Geol. Soc. Lond.* **159**, no. 3, 263–272, doi: [10.1144/0016-764901-046](https://doi.org/10.1144/0016-764901-046).
- Mouslopoulou, V., D. Moraetis, L. Benedetti, V. Guillou, O. Bellier, and D. Hristopulos (2014). Normal faulting in the forearc of the Hellenic subduction margin: Paleoseismic history and kinematics of the Spili fault, Crete, Greece, *J. Struct. Geol.* **66**, 298–308.
- Mouslopoulou, V., A. Nicol, J. J. Walsh, J. G. Begg, D. B. Townsend, and D. T. Hristopulos (2012). Fault-slip accumulation in an active rift over thousands to millions of years and the importance of paleoseismic sampling, *J. Struct. Geol.* **36**, 71–80.
- Mouslopoulou, V., V. Saltogianni, A. Nicol, O. Oncken, J. Begg, A. Babeyko, S. Cesca, and M. Moreno (2019). Breaking a subduction termination from top to bottom: The large M 7.8 Kaikōura earthquake, *Earth Planet. Sci. Lett.* **506**, 221–230.
- Mouslopoulou, V., J. J. Walsh, and A. Nicol (2009). Fault displacement rates over a range of timescales, *Earth Planet. Sci. Lett.* **278**, 186–197.
- Mozafari, N., D. Tikhomirov, O. Sumer, C. Ozkaymak, B. Uzel, S. Yesilyurt, S. Ivy-Ochs, C. Vockenhuber, H. Sozibilir, and N. Akcar (2019). Dating of active normal fault scarps in the Büyük Menderes Graben (western Anatolia) and its implications for seismic history, *Quaternary Sci. Rev.* **220**, 111–123.
- National Observatory of Athens (NOA), Institute of Geodynamics, Athens (1997). National Observatory of Athens Seismic Network, International Federation of Digital Seismograph Networks. Dataset/Seismic Network, Athens, Greece, doi: [10.7914/SN/HL](https://doi.org/10.7914/SN/HL).
- Nicol, A., and L. M. Wallace (2007). Temporal stability of deformation rates: Comparison of geological and geodetic observations, Hikurangi subduction margin, New Zealand, *Earth Planet. Sci. Lett.* **258**, 397–413.
- Nicol, A., R. Van Dissen, Stirling, and M. Gerstenberger (2016). Completeness of the paleoseismic active fault record in New Zealand, *Seismol. Res. Lett.* **86**, 1299–1310, doi: [10.1785/0220160088](https://doi.org/10.1785/0220160088).
- Papadimitriou, P., N. Voulgaris, I. Kassaras, G. Kaviris, N. Delibasis, and K. Makropoulos (2002). The $M_w = 6.0$, 7 September 1999 Athens earthquake, *Nat. Hazards* **27**, 15–33.
- Papanikolaou, D., and I. Papanikolaou (2007). Geological, geomorphological and tectonic structure of NE Attica and seismic hazard implications for the northern edge of the Athens plain, *Bull. Geol. Soc. Greece* **40**, 425–438, doi: [10.12681/bgsg.16634](https://doi.org/10.12681/bgsg.16634).
- Papanikolaou, D., G. Chronis, V. Likousis, and P. Pavlakis (1989). Submarine Neotectonic Map of Saronikos Gulf, E.P.P.O.—N.C.M.R. and Department of Dynamic, Tectonic, Applied Geology (University of Athens), Athens, Greece, Report & map sheet, scale 1:100, 000 (in Greek).
- Papanikolaou, D., S. Lozios, C. Sideris, H. Kranis, G. Danamos, K. Soukis, E. Skourtsos, E. Bassi, P. Marinos, Tsiampaos, et al. (2002). Geological–Geotechnical study of Athens basin, in *OASP Applied Research Program*, OASP, Athens, Greece, 152 pp.
- Papanikolaou, D., V. Lykousis, G. Chronis, and P. Pavlakis (1988). A comparative study of neotectonic basins across the Hellenic arc: Messiniakos, Argolikos, Saronikos and Southern Evoikos Gulfs, *Basin Res.* **1**, 167–176.
- Papazachos, B. C., and K. Papazachou (2003). *The Earthquakes of Greece*, Ziti editions, Thessaloniki, Greece.
- Papazachos, B. C., V. G. Karakostas, C. B. Papazachos, and E. M. Scordilis (2000). The geometry of the Wadati–Benioff zone and lithospheric kinematics in the Hellenic arc, *Tectonophysics* **319**, 275–300.
- Pavlidis, S. B., G. Papadopoulos, and A. Ganas (2002). The fault that caused the Athens September 1999 $M_s = 5.9$ earthquake: Field observations, *Nat. Hazards* **27**, 61–84.

- Pe-Piper, G., and D. J. W. Piper (2005). The South Aegean active volcanic arc: Relationships between magmatism and tectonics, in *Developments in Volcanology*, M. Fytikas and G. E. Vougioukalakis (Editors), 7, no. C, 113–133, doi: [10.1016/S1871-644X\(05\)80034-8](https://doi.org/10.1016/S1871-644X(05)80034-8).
- Roumelioti, Z., D. Dreger, A. Kiratzi, and N. Theodoulidis (2003). Slip distribution of the 7 September 1999 Athens earthquake inferred from an empirical Green's function study, *Bull. Seismol. Soc. Am.* **93**, 775–782.
- Roumelioti, Z., A. Kiratzi, and N. Theodoulidis (2004). Stochastic strong ground-motion simulation of the 7 September Athens (Greece) earthquake, *Bull. Seismol. Soc. Am.* **94**, 1036–1052.
- Roumelioti, Z., A. Kiratzi, N. Theodoulidis, I. Kalogeras, and G. Stavrakakis (2003). Rupture directivity during the September 7, 1999 Athens (Greece) earthquake inferred from forward modeling of strong ground motion, *Pure Appl. Geophys.* **160**, 2301–2318.
- Sakellariou, D., V. Lykousis, S. Alexandri, H. Kaberi, G. Rousakis, P. Nomikou, P. Georgiou, and D. Ballas (2007). Faulting, seismic, stratigraphic architecture and late Quaternary evolution of the Gulf of Alkyonides Basin–East Gulf of Corinth, central Greece, *Basin Res.* **19**, 273–295.
- Sboras, S., A. Ganas, and S. Pavlides (2010). Morphotectonic analysis of the neotectonic and active faults of Beotia (central Greece) using GIS techniques, *Bull. Geol. Soc. Greece* **43**, no. 3, 1607–1618, doi: [10.12681/bgsg.11335](https://doi.org/10.12681/bgsg.11335).
- Schorlemmer, D., S. Wiemer, and M. Wyss (2005). Variations in earthquake-size distribution across different stress regimes, *Nature* **437**, 539–542, doi: [10.1038/nature04094](https://doi.org/10.1038/nature04094).
- Shearer, P. (1997). Improving local earthquake locations using the L1 norm and waveform cross correlation: application to the Whittier Narrows, California, aftershock sequence, *J. Geophys. Res.* **102**, no. B4, 8269–8283.
- Shen, Z., D. D. Jackson, and B. X. Ge (1996). Crustal deformation across and beyond the Los Angeles Basin from geodetic measurements, *J. Geophys. Res.* **101**, 27,957–27,980.
- Stefatos, A., G. Papatheodorou, G. Ferentinis, M. Leeder, and R. Collier (2002). Seismic reflection imaging of active offshore faults in the Gulf of Corinth: Their seismotectonic significance, *Basin Res.* **14**, no. 4, 487–502, doi: [10.1046/j.1365-2117.2002.00176.x](https://doi.org/10.1046/j.1365-2117.2002.00176.x).
- Talebian, M., A. Copley, M. Fattahi, M. Ghorashi, J. Jackson, H. Nazari, R. Sloan, and R. T. Walker (2016). Active faulting within a megacity: The geometry and slip rate of the Pardisan thrust in central Tehran, Iran, *Geophys. J. Int.* **207**, no. 3, 1688–1699, doi: [10.1093/gji/ggw347](https://doi.org/10.1093/gji/ggw347).
- Tselentis, A., and J. Zahradnik (2000). Aftershock monitoring of the Athens earthquake of 7 September 1999, *Seismol. Res. Lett.* **71**, no. 3, 330–337.
- Tsodoulos, I. M., I. K. Koukouvelas, and S. Pavlides (2008). Tectonic geomorphology of the easternmost extension of the Gulf of Corinth (Beotia, Central Greece), *Tectonophysics* **453**, 211–232.
- Veliz, V., V. Mouslopoulou, A. Nicol, B. Fassoulas, J. Begg, and O. Onkcen (2018). Millennial to million year normal-fault interactions on the forearc of a subduction margin, Crete, Greece, *J. Struct. Geol.* **113**, 225–241, doi: [10.1016/j.jsg.2018.05.019](https://doi.org/10.1016/j.jsg.2018.05.019).
- Waldhauser, F. (2001). HypoDD: A program to compute double-difference hypocentre locations, *U. S. Geol. Surv. Open-File Rept.* *01-113*, 1–25.
- Waldhauser, F., and W. L. Ellsworth (2000). A double-difference earthquake location algorithm: Method and application to the northern Hayward fault, California, *Bull. Seismol. Soc. Am.* **90**, no. 6, 1353–1368.
- Wells, D. L., and K. J. Coppersmith (1994). New empirical relationships among magnitude, rupture length, rupture width, rupture area and surface displacement, *Bull. Seismol. Soc. Am.* **8**, 974–1002.
- Wesnousky, S. G. (2006). Predicting the endpoints of earthquake ruptures, *Nature* **444**, 358–360, doi: [10.1038/nature05275](https://doi.org/10.1038/nature05275).
- Wesnousky, S. G. (2008). Displacement and geometrical characteristics of earthquake surface ruptures: Issues and implications for seismic-hazard analysis and the process of earthquake rupture, *Bull. Seismol. Soc. Am.* **98**, 1609–1632, doi: [10.1785/0120070111](https://doi.org/10.1785/0120070111).
- Woessner, J., and S. Wiemer (2005). Assessing the quality of earthquake catalogues: Estimating the magnitude of completeness and its uncertainty, *Bull. Seismol. Soc. Am.* **95**, 684–698, doi: [10.1785/0120040007](https://doi.org/10.1785/0120040007).
- Xu, X., D. T. Sandwell, and B. Smith-Konter (2020). Coseismic displacements and surface fractures from Sentinel-1 InSAR: 2019 Ridgecrest earthquakes, *Seismol. Res. Lett.* doi: [10.1785/0220190275](https://doi.org/10.1785/0220190275).

Manuscript received 20 January 2020

Published online 2 June 2020